IN-FLIGHT ICING SIMULATION ON ENGINE NACELLES

A THESIS SUBMITTED TO
THE GRADUATE SCHOOL OF NATURAL AND APPLIED SCIENCES
OF
MIDDLE EAST TECHNICAL UNIVERSITY

BY

NERMİN UĞUR

IN PARTIAL FULFILLMENT OF THE REQUIREMENTS
FOR
THE DEGREE OF MASTER OF SCIENCE
IN
AEROSPACE ENGINEERING

SEPTEMBER, 2017

Approval of the thesis:

IN-FLIGHT ICING SIMULATION ON ENGINE NACELLES

submitted by **NERMİN UĞUR** in partial fulfillment of the requirements for the degree of **Master of Science in Aerospace Engineering Department, Middle East Technical University** by,

Prof. Dr. Gülbin Dural Ünver
Dean, Graduate School of **Natural and Applied Sciences**

Prof. Dr. Ozan Tekinalp
Head of Department, **Aerospace Engineering**

Prof. Dr. Serkan Özgen
Supervisor, **Aerospace Engineering Department, METU**

Examining Committee Members

Prof. Dr. İsmail Hakkı Tuncer
Aerospace Engineering Department, METU

Prof. Dr. Serkan Özgen
Aerospace Engineering Department, METU

Prof. Dr. Yusuf Özyörük
Aerospace Engineering Department, METU

Prof. Dr. Zafer Dursunkaya
Mechanical Engineering Department, METU

Assoc. Prof. Dr. Kürşad Melih Güleren
Department of Flight Training, Anadolu University

Date: 06.09.2017

I hereby declare that all information in this document has been obtained and presented in accordance with academic rules and ethical conduct. I also declare that, as required by these rules and conduct, I have fully cited and referenced all material and results that are not original to this work.

Name, Last name: Nermin UĞUR

Signature:

ABSTRACT

IN-FLIGHT ICING SIMULATION ON ENGINE NACELLES

Uğur, Nermin
M.S., Department of Aerospace Engineering
Supervisor: Prof. Dr. Serkan Özgen

September 2017, 99 pages

In-flight ice accumulation on airframes may lead to great risks for flight safety due to aerodynamic performance degradation, loss of control, engine rollback and increase in weight. Certification concerns become an important topic when flight safety is considered. To prove that an aircraft can fly safely in certain icing conditions, authorities like FAA and EASA have defined meteorological conditions. Flight tests, laboratory tests and numerical simulations are the methods utilized to show compliance with icing related certification requirements. Besides certification purposes, design of an anti/de-icing systems requires predictions of accumulated ice mass on airframes and its impingement limits for given flight conditions.

The present study aims to develop a computational tool for icing simulations on engine nacelles. The code is written in FORTRAN language and mainly consists of four modules: flow field solution with panel method, droplet trajectory and collection efficiency calculations using Lagrangian approach, thermodynamic analysis for heat transfer coefficient calculations and ice accretion model with Extended Messinger

Model. Icing analyses on two-dimensional wing and engine intake geometries are performed with the developed tool. The results are validated with experimental and numerical data available in literature. Ice shape predictions, collection efficiency and heat transfer coefficient results obtained in the current study are mostly in good agreement with reference results for airfoil and axisymmetric engine intake cases. On the other hand, for non-axisymmetric engine intake geometries, two-dimensional approach is found insufficient when ice shape and impingement limit results are considered. In order to obtain more accurate ice shapes formed on non-axisymmetric engine intakes, three-dimensional approach is suggested despite higher CPU time.

Keywords: In-flight Simulation, Engine Intake, Axisymmetric Intake, Non-axisymmetric Intake, Extended Messinger Model, Airworthiness Certification

ÖZ

HAVA ALIĞI ÜZERİNDE UÇUŞ ESNASINDA BUZLANMA SİMÜLASYONU

Uğur, Nermin
Yükseklisans, Havacılık ve Uzay Mühendisliği Bölümü
Tez yöneticisi: Prof. Dr. Serkan Özgen

Eylül 2017, 99 sayfa

Uçuş esnasında uçak bileşenleri üzerinde meydana gelen buzlanma, aerodinamik performansın düşüşüne, kontrol kaybına, motor arızalarına ve ağırlık artışına neden olması sebebiyle uçuş emniyeti açısından büyük bir risk oluşturmaktadır. Uçuş emniyeti göz önünde bulundurulduğunda sertifikasyon konusu önemli bir yer teşkil eder. Bir hava aracının güvenli bir şekilde uçabileceğini gösterdiği buzlanma koşulları, FAA ve EASA gibi otoriteler tarafından belirlenir. Sertifikasyon gereksinimlerine uyum gösterimi açısından uçuş testleri, laboratuvar testleri ve sayısal simülasyon gibi metotlardan yararlanılır. Sertifikasyon ihtiyaçlarının yanı sıra, buzlanmayı önleyici/giderici sistemlerin tasarımı için de yüzey üzerinde oluşan buz kütlesi ve buzlanma limiti tahminlerine ihtiyaç duyulur.

Bu çalışma, motor hava alığı geometrisi üzerinde buzlanma simülasyonu yapacak olan bir hesaplama aracı geliştirmeyi amaçlamaktadır. FORTRAN dilinde yazılmış olan kod dört ana modülden oluşur: panel metodu ile akış çözümü, Lagrange yaklaşımı ile damlacık yörünge ve birikme etkinliği hesaplamaları, ısı transferi katsayılarının hesaplanması için termodinamik analizler ve Genişletilmiş Messinger Modeli ile buz birikme hesaplamaları. Geliştirilen bu hesaplama aracı ile iki boyutlu kanat ve hava alığı geometrileri üzerinde buzlanma hesaplamaları yapılmıştır. Sonuçlar literatürde yer alan deneysel ve sayısal veriler ile doğrulanmıştır. Mevcut çalışmada elde edilen buz şekli tahminleri, toplanma etkinliği ve ısı transferi katsayıları sonuçları, kanat profili ve eksenel simetrik hava alığı geometrilerinde referans veriler ile çoğunlukla uyumludur. Ancak, eksenel simetrik olmayan hava alığı buzlanma sonuçları iki boyutlu yaklaşımın, buz şekli ve buzlanma limitleri göz önünde bulundurulduğunda yeterli doğrulukta sonuçlar vermediğini göstermiştir. Eksenel simetrik olmayan hava alığı geometrilerinde daha doğru buzlanma sonuçları elde etmek için uzun hesaplama süresine rağmen üç boyutlu bir yaklaşım tercih edilmelidir.

Anahtar kelimeler: Uçus Sırasında Buzlanma Simülasyonu, Hava Alığı, Eksenel Simetrik Hava Alığı, Eksenel Simetrik Olmayan Hava Alığı, Genişletilmiş Messinger Modeli, Uçuşa Elverişlilik Sertifikasyonu

to my family

for their love, care and support

ACKNOWLEDGEMENTS

This study is supported by the Ministry of Science, Industry and Technology of Turkey under the grant 0046.STZ.2013-1. The project partners are Middle East Technical University (METU) and TUSAŞ Engine Industries (TEI). I appreciate all the support given by the Ministry of Science, Industry and Technology of Turkey and the partners.

I would like to express my appreciation to my supervisor Prof. Dr. Serkan Özgen for his supervision, guidance, discussions, which helped me to develop a wider point of view and for sharing his knowledge and experience with me. It was a great chance to work with him.

I would like to thank my friends Tilbe Mutluay and Nazlı Demir for their endless support, love and understanding from the other side of the world. I would like to give special thanks to Tuğçe Kayı who has been beside me since high school with her endless love, support and invaluable friendship. I am also thankful to my friends Arda Çalışkan, Ali Can Özer, Sena Yazırlı, Yakut Cansev Küçükosman, Ilgaz Doğa Okcu, Emrehan Kocabaş, Güçlü Özcan, Samet Emre Yılmaz, Kadircan Kopşa, Başar Kütükoğlu, Mustafa Can Karadayı, Alpay Sancar, Tuanna Demir, Yiğit Atılgan and Selim Yürekli to be there for me from the beginning of our bachelor study. Besides, I would like to express my very great appreciation to Özgür Yalçın and Ayşe Hazal Altuğ who motivated and supported me when I needed the most. I would like also to thank Selin Ece Zıraman, Sırma Damla User and Onur Demir for their friendship and support.

I would also like to thank my colleagues at Turkish Aerospace Industries Inc., especially Erinç Erdoğan and Erhan Feyzioğlu for sharing their experiences and suggestions.

I would like to express my deepest appreciation to my family who gives infinite support, courage and love every single day. It would be impossible to achieve any of these without them.

TABLE OF CONTENTS

LIST OF TABLES

TABLES

LIST OF FIGURES

FIGURES

LIST OF ABBREVIATIONS

Abbreviations

EASA	European Aviation Safety Agency
FAA	Federal Aviation Administration
FAR	Federal Aviation Regulation
LWC	Liquid Water Content
MVD	Median Volumetric Diameter
NACA	National Advisory Committee for Aeronautics
NASA	National Aeronautics and Space Administration
ONERA	French Aerospace Research Center
SLD	Supercooled Large Droplets

Nomenclature

A_p	cross sectional area of particle
A_s	surface area of particle
B, h	ice and water layer thicknesses
c	chord
C_D	drag coefficient of cloud particle
C_p	specific heat at constant pressure
d_p	particle diameter
D	drag force of cloud particle
e	particle eccentricity

h_t	heat transfer coefficient
k	thermal conductivity
k_s	roughness height
L_f	latent heat of freezing
$\dot{m}$	mass flow rate
Pr	Prandtl number
Re	Reynolds number
Re_k	roughness Reynolds number
s	circumferential distance along the geometry surface
Sc	Schmidt number
St	Stanton number
t	time
T	temperature in the ice layer
U_e	edge velocity
U_k	flow velocity at the roughness location
V_{rel}	particle relative velocity
V_∞	freestream velocity
V_x, V_y	velocity vector components of the flow field
$\dot{x}_p, \dot{y}_p$	velocity vector components of the cloud particle
$\ddot{x}_p, \ddot{y}_p$	acceleration vector components of the cloud particle
x,y	Cartesian coordinates
x_p, y_p	position vector components of the cloud particle

Greek symbols

β	local collection efficiency
γ	angle between velocity vectors of the cloud particle and flow field
δ	boundary layer thickness
θ	temperature in the water layer or momentum thickness
μ	dynamic viscosity

v	kinematic viscosity
ρ	density of air or liquid water content
σ_w	surface tension of water
τ	shear stress

Subscripts

a	air properties
f	quantities related to freezing
i	ice properties
imp	quantities related to impinging particles in quantities related to inflowing runback water
k	airflow properties at roughness height
p	particle
sta	static
sub	quantities related to sublimation
tot	total
tr	transition
turb	turbulent
w	water properties

CHAPTER 1

INTRODUCTION

In this chapter, hazards caused by in-flight icing on airframes and the importance of icing simulations in order to avoid these hazards are explained. Firstly, motivation for this study is summarized. After presenting literature survey related to this work, scope and content of the thesis are introduced.

1.1 MOTIVATION

In-flight icing on airframes poses a great danger and it is one of the most important problems in aviation. Ice accumulation may cause several problems during flight such as aerodynamic degradation, loss of control, engine rollbacks and increase in weight. When ice is accreted on airframes, it destroys the smooth flow of the air by degrading aerodynamic profile of the frame which leads to decrease in lift and increase in drag forces. Aircraft may be subject to uncontrollable roll or pitch, where the recovery may not be possible. A blocked intake due to ice formation causes reduction in engine performance. An example of ice accumulation on an engine nacelle is shown in Figure 1. Although it is a secondary effect of icing when compared to the effect on aerodynamic performance, it leads to increase in weight due to accumulation on airframe components. In addition to these, ice accumulation on flight sensors result in false readings of flight data which is a great threat for flight safety.

Figure 1: An example of ice accumulation on an engine nacelle [13]

When it comes to flight safety, icing certification becomes an important topic. Icing conditions at which the aircraft can fly safely are defined by the certification authorities like FAA (Federal Aviation Administration) and EASA (European Aviation Safety Agency). Meteorological conditions for certification compliance include Supercooled Droplets in Appendix C, Supercooled Large Droplets in Appendix O and Mixed Phase and Ice Crystals in Appendix P of FAR (Federal Aviation Regulations), Part 25 and Certification Specifications CS-25 of EASA. Certification process may involve flight tests, laboratory tests or numerical simulations as means of compliance.

Besides certification concerns, prediction of ice accumulation during flight is important in terms of anti/de-icing system design. To estimate the ice mass that will accumulate on the airframe and the impingement limits of the ice accurately will lead to a better design for an anti/de-icing system.

In the light of all these, one can say that it is very crucial to estimate ice accumulation on an airframe for a given icing condition. When the means of estimation are considered, numerical simulation helps to scan a wider range of icing conditions more easily than flight and laboratory tests which are required by certification compliance.

Although it is not a matter of question to fully replace flight and laboratory tests, numerical simulation tools certainly reduce the demand for them.

1.2 LITERATURE SURVEY

Study presented by Myers [15] is prominent in icing field, since it introduces the Extended Messinger Model, which is used by many icing analyses software. With this extension, deficiencies of the original model are eliminated and ice accretion prediction accuracy is improved. Mathematical models for rime ice and glaze ice are introduced. The comparison between Original and Extended Messinger model exists in terms of ice growth rates and freezing fractions. The one-dimensional model that is introduced is also extended to two and three dimensions.

Using Extended Messinger Model as a base, ice accretion is simulated on a multi-element airfoil in two-dimensions in the study of Özgen and Canıbek [18]. Ice shape predictions are obtained with the developed tool and compared with both numerical and experimental literature data. Moreover, effect of different parameters like chord length, droplet diameter, velocity and angle of attack on collection efficiency is presented in this study.

In another study of the same authors [19], same procedure for 2D in-flight icing simulations as in Reference [18] on SA 13112 airfoil profile is applied. Additionally, the effect of compressibility on ice shape predictions is studied. The results for different Mach regimes are present. In this study, it is deduced that compressibility has an important effect on the ice mass accumulated and also the region which is subject to icing.

3D icing simulations where droplet trajectories are achieved with Lagrangian approach are presented in the studies of Özgen et al [21]. Parallelization is used in the computational procedure. Flow field solution is obtained by utilizing three-dimensional panel method. Analyses on wing geometries are done for different test cases and the results are compared with both numerical and experimental data available in the literature.

The study presented by Özgen and Canıbek [22] is an effort to simulate ice accretion in two and three dimensions for airfoil and wing geometries. Moreover, ice accretion on circular, elliptical and turboprop trainer intakes are investigated. Icing analyses are conducted for different test cases and results are compared with numerical and experimental data.

Collection efficiency analysis for a business jet tail geometry is presented in the study of Özgen et al [23]. The analyses are conducted for different angles of attack by including SLD (Supercooled Large Droplets) effects like droplet breakup, splash, bounce and non-spherical droplets.

Both numerical and experimental studies on icing have been carried on by NASA since 1980s. Experiments have been conducted in Icing Research Tunnel at NASA Glenn Research Center, which have been great references in the icing field. Additionally, LEWICE software, which is developed by NASA Lewis Research Center, is a pioneer of numerical icing analyses. Various reports including the results of these experiments and numerical analyses have been published. For example, the study presented by Papadakis et al [26] is an important reference with experimental and numerical data related to icing analyses on different geometries like airfoils, finite wing sections and an S-duct engine inlet. In this report, impingement characteristics of droplets with different diameter, collection efficiencies and corresponding ice shape predictions obtained in the experiments are presented. Experimental results are compared with numerical results which are obtained with LEWICE-2 and LEWICE-3 software. Since reference data related to engine inlet is very scarce in the literature, this study is an invaluable source in order to validate the results obtained in this thesis.

Another NASA report was published by Wright and Potapczuk [32], which is related to modeling physics of SLD during icing. The characteristics of SLD such as breakup and splash and their effects on icing analyses of MS-317 airfoil profile and a three section multi-element airfoil are included in this report. Collection efficiency, ice shape and ice mass results are compared with experimental data.

Validation results of LEWICE 3.0, which is a software developed by NASA, are presented by Wright [33]. Parameters related to collection efficiency such as maximum collection efficiency, total collection efficiency, upper and lower impingement limits and the location on the upper and lower surface where collection efficiency reaches 10% are shown in this report. Furthermore, Wright published another report [34], which presents the refinements of SLD model for LEWICE. Collection efficiency and ice shape results are shown and compared with experimental data.

Wright et al [37] present their study on modeling ice crystals and mixed phase icing on a turbofan engine. In this paper, the effects of phase change and temperature change are added to the trajectory model. Moreover, non-spherical ice crystals and a model for ice erosion are also included. Although the results are not compared with experimental data, this reference is an important source both for icing modeling of engines and validation studies performed.

Eulerian approach is proposed for droplet trajectory calculations by Iuliano et al [14]. Eulerian method provides more accurate results than Lagrangian method when icing analyses on complex geometries are considered. In this study, three-dimensional icing analyses on an axisymmetric nacelle and a horizontal swept tail are performed. Collection efficiencies are obtained for various test cases. The results are validated with experimental data where good agreement is observed. This reference is important when it is considered that it proposes Eulerian method for droplet trajectories and numerical data for engine nacelle which is scarce in the literature.

Dima and Brandi [9] present icing analyses on single and multi-element airfoils which are performed with CIRA Multi-Ice Code. Ice shape prediction results are compared with other similar code results and experimental data.

A multi-stage jet engine is analyzed in terms of ice accretion in the study of Veillard et al [30]. Flow field solution, droplet impingement, heat transfer coefficient and ice accretion calculations are achieved through different modules in FENSAP-ICE code. A three-dimensional quasi-steady approach is proposed both for rotating and static components. At first, the approach is validated for Aachen turbine. Later, collection efficiency and ice shape predictions belonging to different parts are presented.

Bidwell [4] performed icing analyses on low pressure compressor of the E3 (Energy Efficient Engine). Flow field solution, droplet trajectories and ice accretion on compressor components are presented for E3. Computations are performed for various droplet diameters. Ice shape predictions are obtained for 20 µm Langmuir-D distribution and for a 92 µm SLD distribution with and without splashing cases. Both rotating and non-rotating components are considered.

Engine nacelle of Boeing-737-300 is studied in terms of icing analyses by Al-Khalil et al [2]. Since the geometry is not very complex, three-dimensional VSAERO panel code is found to be adequate for flow field solution. Droplet trajectories are computed with ICE code and heat transfer computations are done with ANTICE code. Collection efficiency results are compared with experimental data which are in good agreement.

Hamed et al. [11] presents three-dimensional icing analyses on aeroengine rotating machinery. An Eulerian-Lagrangian approach is used for droplet trajectories. Collection efficiency distributions on the blades are obtained for varying droplet diameters.

A numerical study on three-dimensional icing analyses of an engine inlet is presented by Shen et al [28]. FLUENT software is utilized as the flow solver in this study. Droplet trajectories, heat transfer and ice accretion calculations are performed. Ice shape prediction results of the inlet geometry are shown and compared with the ones obtained with FENSAP-ICE code. It is noticed that the results are in good agreement.

Three-dimensional ice accretion calculations are carried out for a helicopter rotor blade in the study of Beaugendre et al [3] with FENSAP-ICE code. Mathematical models for different modules of the code are explained (FENSAP: flow solver, DROP3D: impingement module, ICE3D: ice accretion module). Ice shape prediction comparisons with experimental and numerical data (ONERA) are presented for different sections of the rotor blade. Moreover, ice shape predictions obtained with ICE3D for NACA0012 airfoil profile are compared with two-dimensional experimental and numerical data (obtained with LEWICE).

In the study of Bourgault et al [6], an Eulerian model is introduced as an alternative to Lagrangian model for droplet trajectories. Collection efficiency analyses are performed for two-dimensional cylinder and three-dimensional sphere geometries and the results are compared with both numerical and experimental data which exist in the literature.

Literature survey helped to decide which methods will be utilized in the icing analyses in the scope of this thesis. For flow field solution, Hess-Smith Panel Method is used which is found sufficient for this study rather than Navier-Stokes solution. Droplet trajectories and collection efficiency calculations are handled with the Lagrangian approach. Thermodynamic analyses are performed with 2-D Integral Boundary Layer Method which is explained by Gent [10]. As the last step of icing simulation, ice accretion modeling is achieved with Extended Messinger Model suggested by Myers [15].

1.3 SCOPE OF THE THESIS

In the present study, two-dimensional icing analyses are performed on engine intakes with the developed computational tool. The results obtained with this computational tool are validated with reference numerical and experimental data which are available in the literature [14], [28]. In addition to engine intake geometries, validation studies on airfoil geometries are performed as well, since significant amount of icing data is available for airfoil geometries that can be used for further validation.

This study is conducted within the scope of a project with the cooperation of TEI and the financial support of Ministry of Science, Industry and Technology of Turkey and TEI (0046.STZ.2013-1). The aim of the project is to develop a software for the analysis of the atmospheric icing problem of aircraft engine components. Developed tool is considered to have the potential of being used for design, development and certification studies in aviation and academic purposes. It is capable of performing 2-D icing analyses on wing geometries and engine intakes. The tool has the ability to include Supercooled Large Droplet (SLD) and high speed effects. The results for ice shape prediction, collection efficiency and heat transfer coefficient distributions on the surface, which are obtained in validation studies are mostly in quite good agreement with the reference data. This thesis includes the studies on 2-D icing analyses on airfoils and engine intakes only.

1.4 CONTENT OF THE THESIS

Chapter 2 includes the physics behind ice formation and ice types, namely rime and glaze ice. Moreover, the factors that affect icing are listed and explained briefly.

In Chapter 3, the methodology applied for 2-D icing analysis is described in detail. The four main steps of the algorithm employed in the computational tool are explained, which are flow field solution, droplet trajectory and collection efficiency calculations, thermodynamic analysis and ice accretion model.

In Chapter 4, Supercooled Large Droplets (SLD) and the phenomena related to them are explained. The differences between SLD and supercooled droplets in terms of computational models are discussed.

Validation studies for airfoil geometries are presented in Chapter 5. Ice shape and collection efficiency results are given for varying icing conditions.

Chapter 6 presents the validation studies performed for icing analyses on different engine intake geometries. Ice shape predictions, collection efficiency distributions and heat transfer coefficients are provided for varying icing conditions.

The last chapter, Chapter 7, summarizes important findings of the thesis and recommendations for future work.

CHAPTER 2

ICING PHYSICS

2.1 ICE FORMATION

Ice formation occurs if ambient temperature is below 0^{o}C and supercooled water droplets are present in the atmosphere. As the water droplets impact on the surface, either all of them or some of them freeze depending on the icing condition. As they freeze, heat is released until the ice surface temperature reaches 0^{o}C. If the case where there exists unfrozen water is considered, it is seen that unfrozen water starts to run back along the surface or accreted ice and freezes at some point downstream. This phenomenon is known as runback ice and it must be modeled for better icing prediction analysis.

Depending on the temperature at which the icing occurs, type of ice differs. There are mainly two types of ice which are rime ice and glaze (clear) ice, which are explained in the following part of the chapter.

2.2 ICE TYPES

2.2.1 Rime ice

Rime ice occurs when water droplets freeze on contact at icing conditions with low airspeed, low temperature and low liquid water content. It is a dry, opaque, crystalline deposit which is quite brittle.

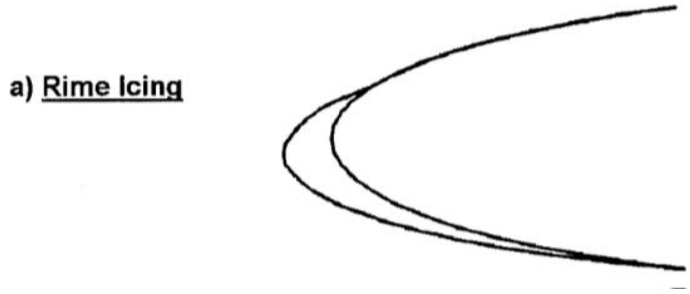

Figure 2: Rime ice formation [1]

Rime ice often forms on leading edges and can affect the aerodynamic qualities of an airfoil or the airflow into the engine intake. It usually forms in such a way that the accumulated ice follows the contour of the surface as seen in Figure 2. Detection and removal of rime ice is easy.

The temperature range for the formation of rime ice can be between 0°C and –40°C, but is most commonly encountered in the range from –10°C to –20°C.

2.2.2 Glaze (clear) ice

Glaze ice forms at temperatures around 0°C and typically at high liquid water content. It occurs when a fraction of the water droplets freezes upon impact while the remainder run back along the surface and freeze downstream. It has a clear appearance and irregular shape like double horned, beak or rounded, which is demonstrated in Figure 3. It is difficult to detect and remove glaze ice accumulated on the surface.

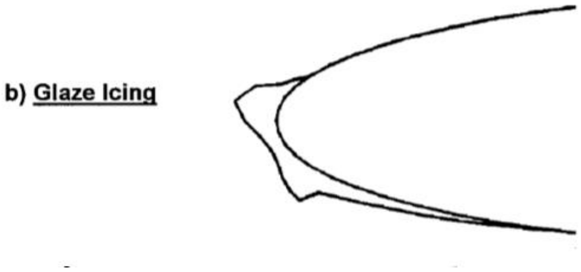

Figure 3: Glaze ice formation [1]

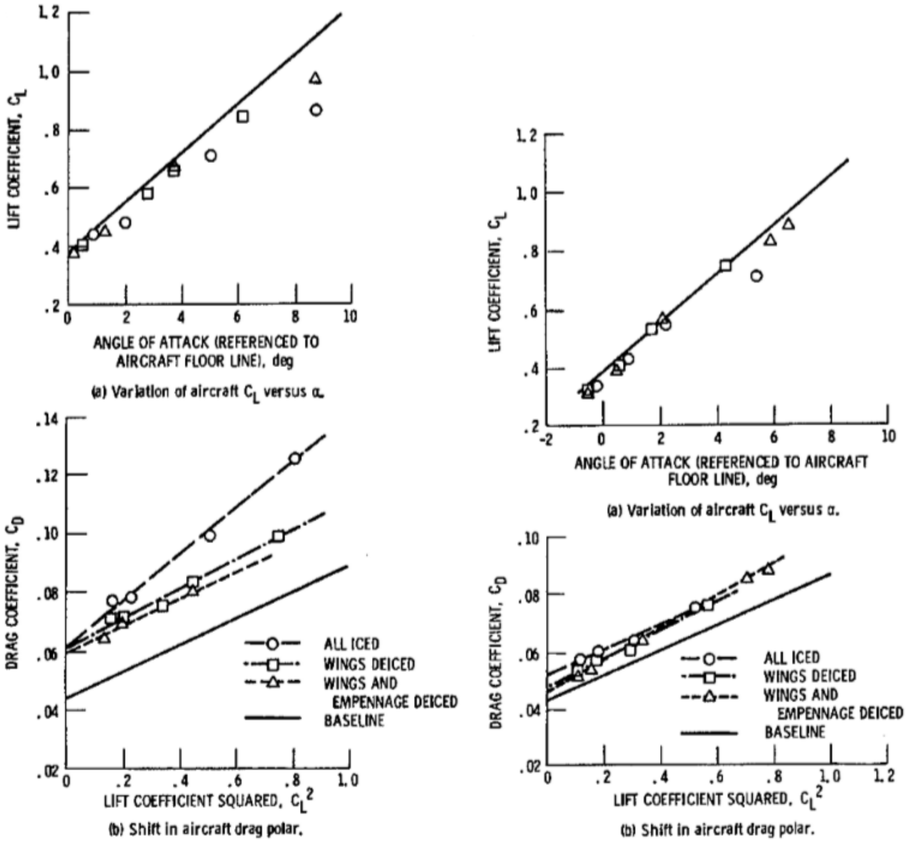

(a) Glaze ice

(b) Rime ice

Figure 4: Effect of icing on aircraft lift curve and drag polar. (a) Glaze ice, (b) Rime ice [1]

Due to its irregular shape, it can alter the aerodynamic shape of the airfoils quite dramatically and reduce their effectiveness. That is why glaze ice is considered to be more detrimental in terms of aerodynamic performance when compared to rime ice. Figure 4 illustrates the effect of glaze and rime ice on lift and drag of NASA Lewis research aircraft. Glaze ice leads to more decrease in lift and more increase in drag than rime ice when compared to baseline (no ice) case.

Another hazard of glaze ice is the possible damage caused by ice pieces which break from the glaze ice bulk. In this case, a study to trace the broken piece and determine whether it will damage any surface is worth to be undertaken.

2.3 FACTORS AFFECTING ICING

2.3.1 Liquid water content

Liquid water content (LWC) is the measure of the mass of the water in a cloud in a specified volume of dry air. It varies for different cloud types and exposure distances for a given temperature and droplet size which are presented in FAR/CS 25 Appendix C.

Figure 5 depicts ice shapes for two different temperature cases with varying LWC values. In both temperature cases, ice mass accumulated on the airfoil increases with increasing LWC.

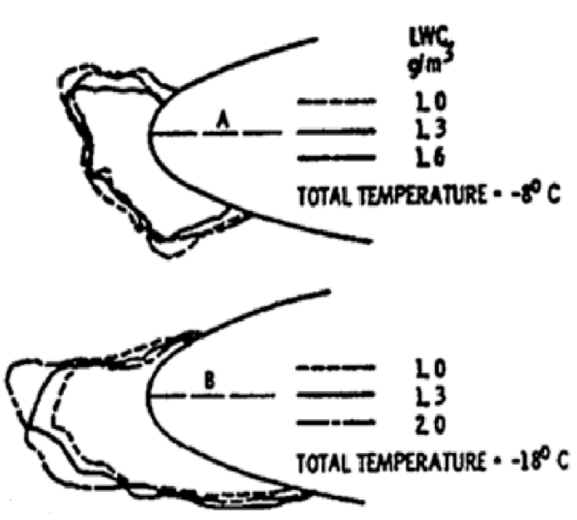

Figure 5: Effect of LWC on ice shape on an airfoil [1]

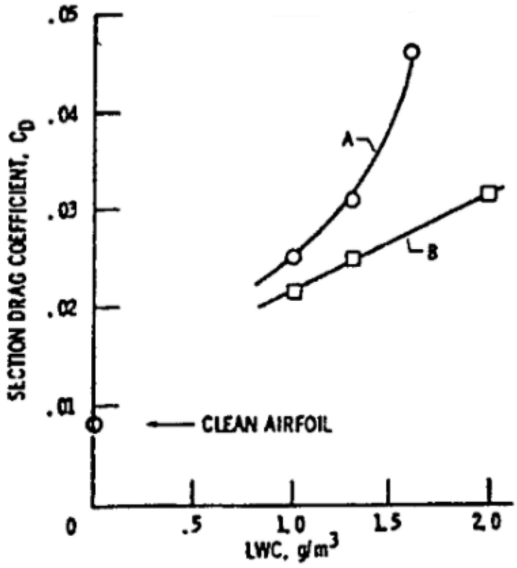

Figure 6: Effect of LWC on section drag [1]

Figure 6 shows the effect of LWC on section drag for different temperature cases A and B as in Figure 5. As seen, for both temperature cases, section drag coefficient increases with increasing LWC due to ice accumulation at the leading edge of the airfoil. However, increase in drag coefficient is steeper for temperature A, which yields a glaze ice shape due to higher temperature, as can be seen in Figure 5.

2.3.2 Temperature

Temperature has a great effect on icing in terms of ice mass accreted, ice type and ice shape formed on the surface.

Figure 7 shows how the ice shape changes with increasing temperature for two different icing conditions. In both conditions, ice is typically rime ice at the lowest temperature and turning into a horn-like shaped glaze ice as temperature increases. As temperature is further increased, ice accumulated on the surface decreases.

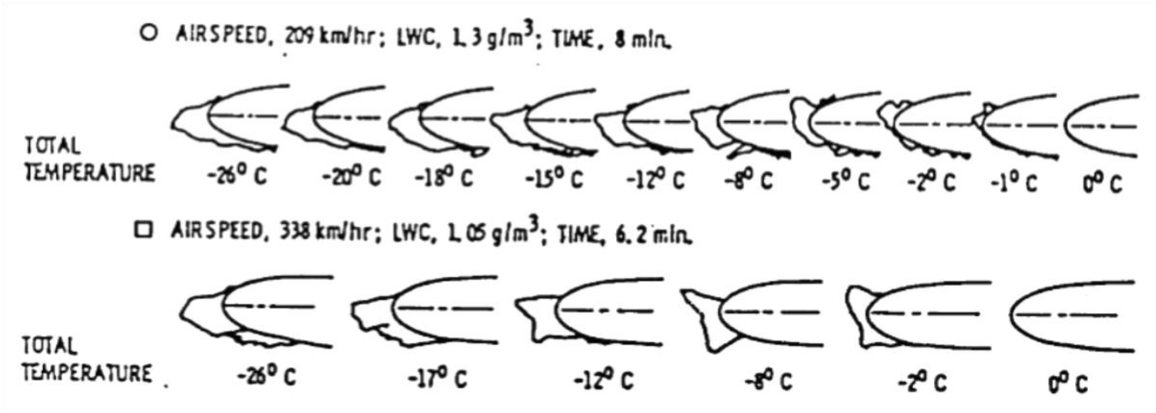

Figure 7: Effect of total temperature on ice shape on an airfoil [1]

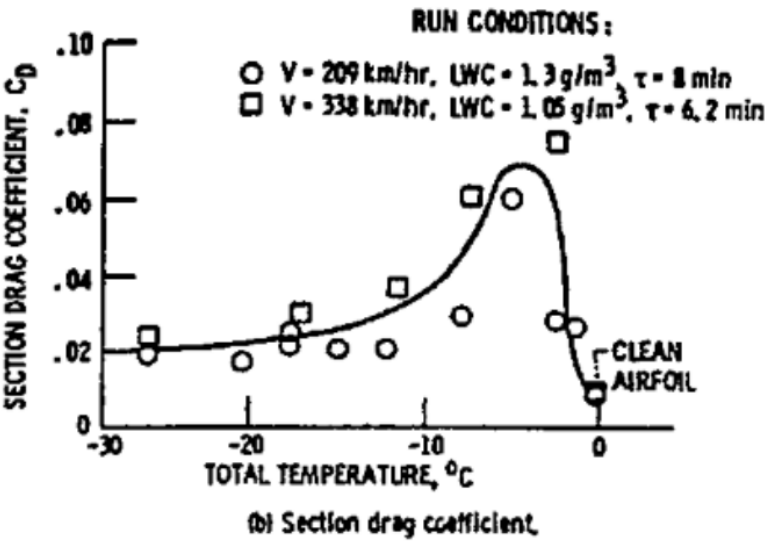

Figure 8: Effect of total temperature on section drag [1]

Section drag coefficient change with temperature for each icing condition in Figure 7 is given in Figure 8. It is seen that the peak drag is observed at around -5°C, which corresponds to glaze ice case where the horns and their effects on the airflow are the largest.

2.3.3 Airspeed

Airspeed is another important factor affecting airframe icing. As airspeed increases, water droplets follow ballistic trajectories since they do not have enough time to deviate from the airframe. Therefore, more droplets impinge on the surface which leads to a wider region with accumulated ice. Moreover, high airspeed is effective on icing due to aerodynamic heating. According to the temperature of the exposed airframe, ice type accreted on the surface changes. Glaze ice is usually observed at high velocities.

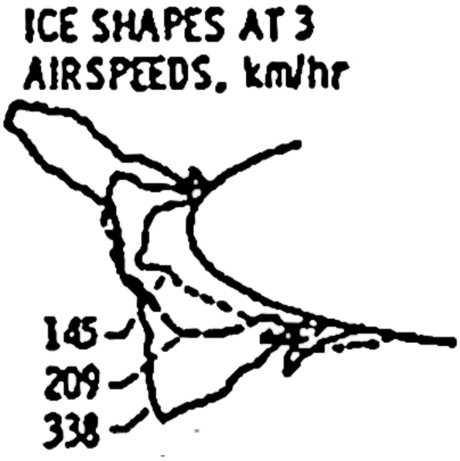

Figure 9: Effect of airspeed on ice shape on an airfoil [1]

Figure 9 shows that ice shape and ice mass changes with varying airspeed values. As airspeed increases, ice mass accumulated on the surface increases and the ice shape shows a glaze ice characteristic with relatively irregular shape.

Figure 10 shows how collection efficiency changes for varying airspeed values. Collection efficiency can be defined as the ratio of the area of impingement to the area through which water passes at some distance upstream of the section.

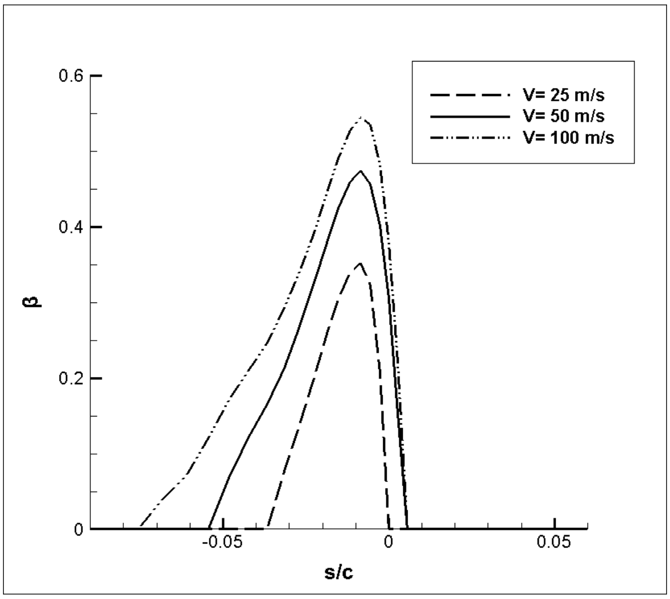

Figure 10: Effect of airspeed on collection efficiency

Collection efficiencies for varying airspeed values are obtained for NACA0012 airfoil with the developed computational tool as in Figure 10. It is observed that not only maximum collection efficiency increases, but also impingement zone gets wider with increasing airspeed. Since angle of attack is 5^o, most of the ice formation occurs on the lower half surface of the airfoil where $s/c < 0$.

2.3.4 Droplet diameter

Droplet size is expressed with median volumetric diameter (MVD) in micrometer. It has a similar effect on icing with airspeed. Since kinetic energy of droplets increases with increasing droplet size, they follow ballistic trajectories and impingement on airframe increases which leads to a wider iced region. Three different icing conditions are shown in Figure 11 for varying droplet size values. It is noticed that ice thickness and impingement limits are significantly larger for larger droplet sizes.

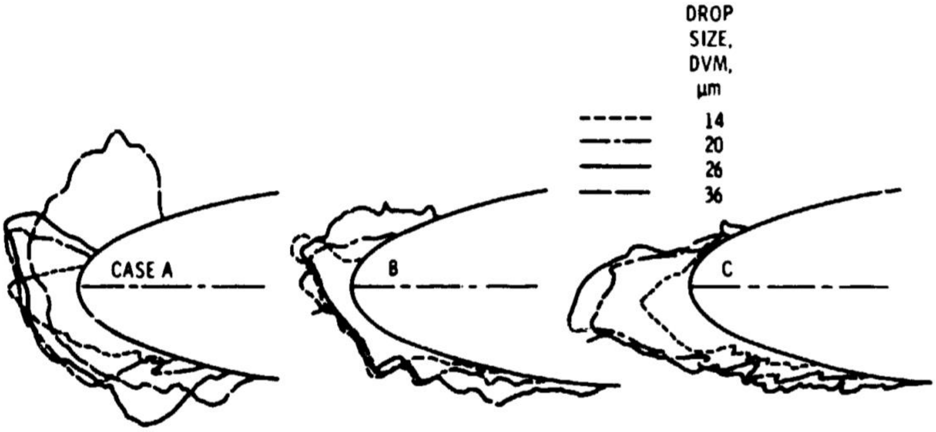

Figure 11: Effect of droplet size on ice shape on an airfoil [1]

In Figure 12, effect of droplet size on collection efficiency on NACA0012 profile is presented with varying droplet sizes. Collection efficiency results are obtained with the developed tool for α=5°. Collection efficiency increases significantly with increasing droplet size. Moreover, as in airspeed case, impingement zone gets wider when droplet size increases.

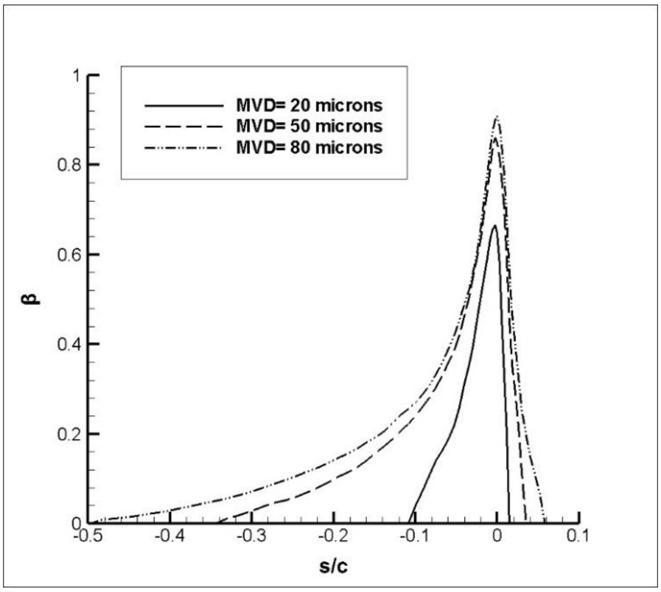

Figure 12:Effect of droplet size on collection efficiency

2.3.5 Airframe size

Airframe size is another factor affecting icing. A larger airframe will be a larger obstacle for the incoming droplets, which will lead them to deviate significantly away from it. Thus, trajectories will roughly follow the streamlines and fewer droplets impact the surface over a narrow impingement zone. In other words, smaller airframes are more prone to icing when compared with larger airframes for the same icing conditions.

Figure 13 shows collection efficiency distribution on NACA0012 profile with 5^o of angle of attack for varying chord lengths. Collection efficiency curves are obtained with the developed computational tool. As chord length gets smaller, collection efficiency increases and ice occupies a wider region on the surface as illustrated.

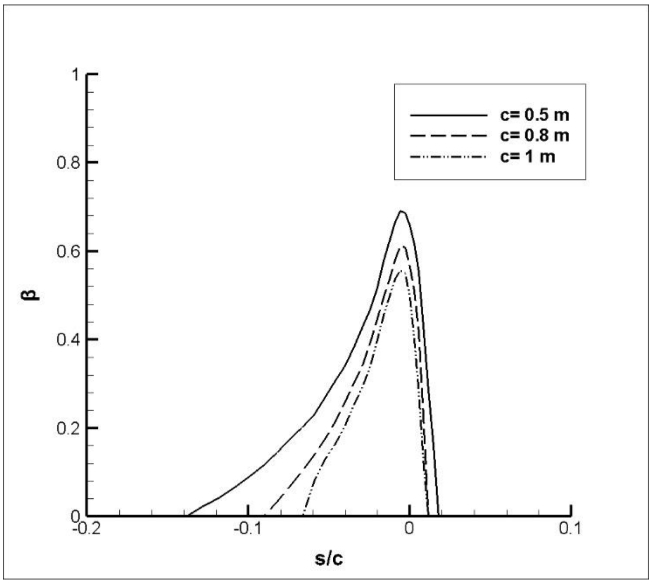

Figure 13: Effect of airframe size on collection efficiency

CHAPTER 3

2-D ICING PREDICTION

In this chapter, four modules of the computational tool, namely the modules for flow field solution, droplet trajectory calculations, thermodynamics and ice accretion are explained respectively.

3.1. FLOW FIELD SOLUTION

Flow solution is needed in order to obtain velocity and pressure distributions on the surface for boundary layer calculations and off-body velocities for trajectory calculations. For these purposes, 2-D Hess-Smith Panel Method is utilized.

According to Hess Smith Panel Method, the geometry is divided into panels which are line segments. Each of these panels has a source singularity which is constant along each panel. In addition, a vortex singularity is defined which is constant for all panels. The strengths of the singularities are taken to be constant along each panel and are unknowns of the problem. Therefore, for a panel method solution with N panels, there exist N unknowns coming from source singularities and 1 unknown from vortex singularity. In total, N+1 unknowns must be found in order to achieve flow field solution with panel method.

Although the flow field solution procedure is straight-forward as explained above for simple geometries like airfoils, it is more complicated when engine intake geometry is considered. It is challenging to maintain both the required flight condition and the required mass flow rate through the intake. The desired mass flow rate is achieved at the control plane which is shown in Figure 14 and it is calculated in terms of the average control plane velocity in x-direction, denoted by $\bar{U}_{cp}$, the control plane area A_{cp}, and the average density $\bar{\rho}_{cp}$.

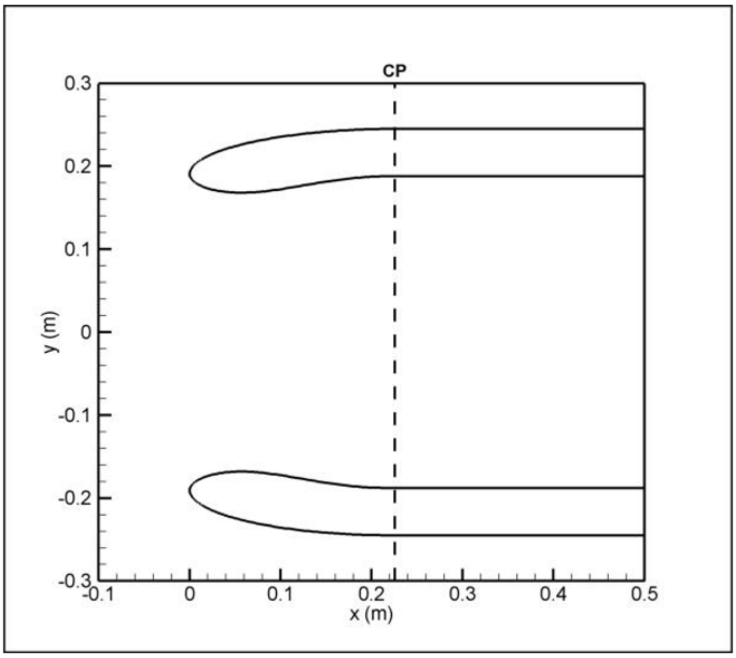

Figure 14: Modified intake geometry for panel method with constant diameter

The average control plane velocity is calculated by taking the average of the x-component of the velocity vector at 30 evenly distributed points along the control plane. In order to correctly enforce the desired mass flow rate as well as the desired freestream velocity, a superposition procedure is applied which is described by Waung [38]. In this method, the panel geometry is modified as shown in Figure 14 by extending the trailing edge panels in x-direction in order to avoid unrealistic velocity gradients at the trailing edge. In this superposition approach, there are two flow situations which are demonstrated in Figure 15.

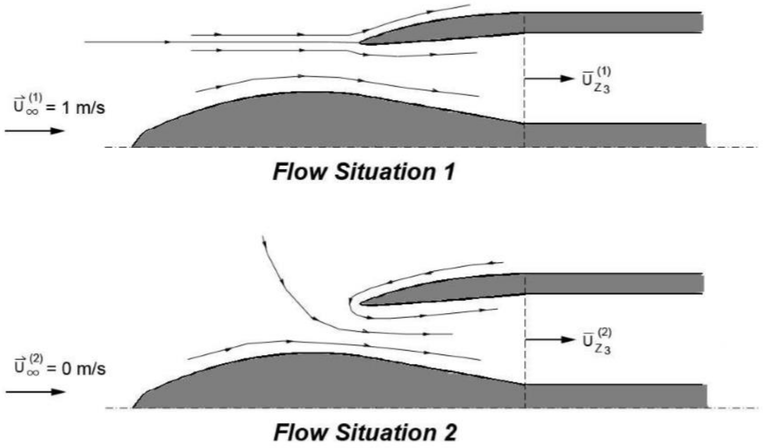

Figure 15: Visual representation of two flow situations used in the superposition method [38]

In the first flow situation, engine intake is operating at $U_\infty = 1$ freestream velocity at $\alpha = 0^o$. The second flow condition is a static flow situation ($U_\infty = 0$) where vortex strength along the surface panels are assigned a value of 1, simulating a flow where the freestream velocity is 0, but there is a non-zero mass flow rate at the control plane. The final flow solution is calculated by scaling and combining these two flow situations.

The solution procedure for each of the flow situations differ slightly. In order to solve flow situation 1, the developed computer program uses N panels to solve for N+1 singularity strengths using the flow tangency boundary condition at the collocation points of the panels. An additional equation is introduced for the Kutta condition, which is enforced at the leading edge of the intake lip. Stagnation point where Kutta condition is applied is found iteratively. Flow situation 2 is solved for $U_\infty = 0$ and Γ=1. Since the vortex strength is no longer an unknown, the developed computer program uses N panels to solve for N source strengths using the flow tangency boundary condition at the collocation points of the panels without any additional boundary conditions.

The solutions of the two flow situations are scaled using the superposition approach. The combination coefficients are solved using the following system of equations:

$$c_1 U_{\infty 1} + c_2 U_{\infty 2} = U_\infty \tag{1}$$

$$c_1 \overline{U}_{cp1} + c_2 \overline{U}_{cp2} = \overline{U}_{cp} \tag{2}$$

Since $U_{\infty 1} = 1$ and $U_{\infty 2} = 0$, it follows that $c_1 = U_\infty$ and $c_2 = (\overline{U}_{cp} - U_\infty \overline{U}_{cp1})/\overline{U}_{cp2}$. Once the singularity strengths are calculated, one can construct a velocity potential and hence calculate the air flow velocity components at any location in the flow field including the boundaries of the geometry. The velocity components at a given point are the x-, y-derivatives of the velocity potential constructed at that point. The results of the panel method also serve the boundary-layer calculations used for the computation of the convective heat transfer coefficients, where the inviscid velocity distribution over the geometry is required. The velocity components are corrected for compressibility effects using the Prandtl-Glauert compressibility correction:

$$\hat{u} = \bar{u}/\sqrt{1 - M^2}\,, \quad \hat{v} = \bar{v}/\sqrt{1 - M^2}, \tag{3}$$

where $\bar{u}$ and $\bar{v}$ are the perturbation velocity components calculated for incompressible flow and $\hat{u}$ and $\hat{v}$ are the same quantities corrected for compressibility effects.

3.2. DROPLET TRAJECTORIES AND COLLECTION EFFICIENCY CALCULATIONS

3.2.1. Droplet Trajectories

The assumptions which are considered for droplet trajectory calculations can be listed as:

- Droplets are assumed to be spherical.
- The flow field is not affected by the droplets.
- Gravity and aerodynamic drag are the only forces acting on the droplets.
- Heat and mass transfer (evaporation) between the droplet and the surrounding flow are neglected.
- The droplet is assumed to have the same temperature as the flow.

Droplet trajectories are obtained using Lagrange approach. The motion of the droplets is defined with the following governing equations:

$$m\ddot{x}_p = -D\, cos\, \gamma \tag{4}$$

$$m\ddot{y}_p = -D \sin\gamma + mg \tag{5}$$

where

$$\gamma = tan^{-1}\frac{\dot{y}_p - V_y}{\dot{x}_p - V_x}, \tag{6}$$

$$D = \frac{1}{2}\rho V_{rel}^2 C_D A_p \tag{7}$$

$$V_{rel} = \sqrt{\left(\dot{x}_p - V_x\right)^2 + \left(\dot{y}_p - V_y\right)^2} \tag{8}$$

In the above equations, V_x and V_y are the flow velocity components at the droplet location, while $\dot{x}_p$, $\dot{y}_p$, $\ddot{x}_p$ and $\ddot{y}_p$ are the components of the droplet velocity and acceleration. The symbols ρ and A_p denote the atmospheric density and cross-sectional area of the droplet. C_D denotes the particle drag coefficient. In the present study, the following formulation is employed for drag coefficients [10]:

$$C_D = \frac{24}{Re}(1 + 0.197Re^{0.63} + 2.6 \cdot 10^{-4}Re^{1.38}) \qquad Re \leq 3500 \tag{9}$$

$$C_D = \frac{24}{Re}(1.699 \cdot 10^{-5})Re^{1.92}, \qquad Re > 3500 \tag{10}$$

In the above formulation, $Re = \rho V_{rel} d_p / \mu$ is the Reynolds number based on droplet diameter d_p and relative velocity V_{rel}. The viscosity μ is calculated using Sutherland's law as a function of temperature.

Trajectory calculations start from an upstream location far away from the leading edge so that air flow velocity components are sufficiently close to their freestream values. The initial droplet velocity is taken to be the terminal velocity as follows:

$$V_{term}^2 = \frac{4}{3}\frac{(\rho_w - \rho)}{\rho}\frac{g d_p}{C_D} \tag{11}$$

The droplet trajectories are obtained by integrating equations (4) and (5) over time until the droplet impacts the geometry or misses it. The droplet impact pattern on the section determines the amount of water that impinges on the surface and the region subject to icing.

3.2.2. Collection Efficiency Calculations

The local collection efficiency is defined as the ratio of the area of impingement to the area through which water passes at some distance upstream of the section which is demonstrated in Figure 16. This distance is taken as 10 times of the chord length in the current study.

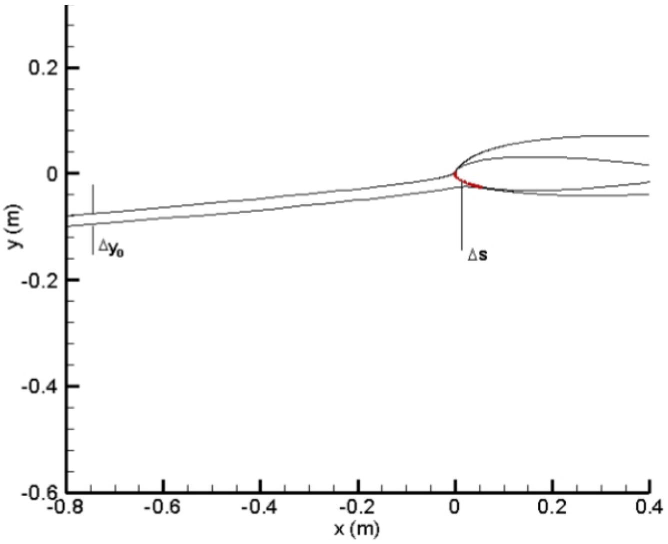

Figure 16: Definition of collection efficiency [17]

The two-dimensional collection efficiency is defined as:

$$\beta = \frac{\Delta y_0}{\Delta s} \tag{12}$$

where Δy_0 is the space between two water droplets at the release plane and Δs is the distance between the impact locations of the same two droplets on the airfoil as seen in Figure 16.

3.3. THERMODYNAMIC ANALYSIS

After flow field and droplet trajectory calculations, convective heat transfer coefficients are needed to be obtained for thermodynamic analysis. The current study employs a 2-D Integral Boundary Layer Method for the calculation of the convective heat transfer coefficients. The boundary-layer calculations start at the stagnation point at the leading edge and proceed downstream using the marching technique for the outer and inner surfaces of geometry.

Transition from laminar to turbulent flow occurs when the Reynolds number based on roughness height Re_k exceeds 600 which is defined as:

$$Re_k = \rho U_k k_s / \mu \tag{13}$$

with k_s being the roughness height and U_k being the local flow velocity at the roughness height which are defined as [27]:

$$k_s = \frac{4\,\sigma_w \mu_w}{\rho_w F\,\tau} \tag{14}$$

$$\frac{U_k}{U_e} = 2\frac{k_s}{\delta} - 2\left(\frac{k_s}{\delta}\right)^3 + \left(\frac{k_s}{\delta}\right)^4 + \frac{1}{6}\frac{\delta^2}{\nu}\frac{dU_e}{ds}\frac{k_s}{\delta}\left(1 - \frac{k_s}{\delta}\right)^3 \tag{15}$$

with σ_w being surface tension, μ_w being viscosity of water, ρ_w is density of water, F is the fraction of airfoil surface wetted by droplets and τ is total shear stress. Moreover, U_e is the flow velocity outside the boundary-layer at the roughness location and s is the streamwise distance along the airfoil surface starting at the stagnation point.

Laminar boundary layer thickness, δ is [27]:

$$\delta = \frac{315}{37}\theta_l \tag{16}$$

θ_l is laminar momentum thickness, defined with Thwaites formulation as [27]:

$$\frac{{\theta_l}^2}{\nu} = \frac{0.45}{{U_e}^6(s)}\int_0^s {U_e}^5(s)\,ds \tag{17}$$

According to the method used by Özgen et al [19], [20], the convective heat transfer coefficients in the laminar flow region are calculated employing the method of Smith and Spaulding [10]:

$$h_c = \frac{0.296kU_e^{1.435}}{\sqrt{\nu \int_0^s U_e^{1.87} ds}} \tag{18}$$

where k is the thermal conductivity of air. The convective heat transfer coefficient in the turbulent region is computed using the method of Kays and Crawford [10]:

$$h_c = St\rho U_e C_p \tag{19}$$

where C_p is the specific heat of air and St is the Stanton number where:

$$St = \frac{C_f/2}{Pr_t + \sqrt{(C_f/2)/St_k}} \tag{20}$$

Turbulent Prandtl number, Pr_t=0.9 and St_k is roughness Stanton number which is:

$$St_k = 1.92{Re_k}^{-0.45}Pr^{-0.8} \tag{21}$$

Laminar Prandtl number, Pr=0.72. Turbulent skin friction is given according to Makkanen relation as [10]:

$$\frac{C_f}{2} = \frac{0.1681}{\left[ln\left(864\frac{\theta_t}{k_s} + 2.568\right)\right]^2} \tag{22}$$

Turbulent momentum thickness is:

$$\theta_t = \frac{0.036\nu^2}{{U_e}^{3.29}}\left(\int_{s_{tr}}^{s} {U_e}^{3.86}(s)ds\right)^{0.8} + \theta_{tr} \tag{23}$$

s_{tr} is transition location where Re_k=600 and θ_{tr} is laminar momentum thickness at $s = s_{tr}$.

3.4. ICE ACCRETION MODEL

The last step of icing prediction analysis is the one where ice accretion is modeled. Icing on a surface is based on a phase change problem or the Stefan problem. It is modeled by applying Extended Messinger Method. Extended Messinger Method differs from Original Messinger Method by including smooth temperature transition between ice and water layer. In Original Messinger Method, the temperature is considered to be constant but different in each of the ice and water layers and there is a discontinuity at the interface. On the other hand, temperature is considered to be continuous between two layers in Extended Messinger Method which is more realistic and gives better results in ice shape prediction [15].

The governing equations for the phase change problem are mainly: energy equations in the ice and water layers, mass conservation equation and a phase change condition at the ice/water interface [15] which are listed below, respectively.

$$\frac{\partial T}{\partial t} = \frac{k_i}{\rho_i C_{pi}} \frac{\partial^2 T}{\partial y^2} \tag{24}$$

$$\frac{\partial \theta}{\partial t} = \frac{k_w}{\rho_w C_{pw}} \frac{\partial^2 \theta}{\partial y^2} \tag{25}$$

$$\rho_i \frac{\partial B}{\partial t} + \rho_w \frac{\partial h}{\partial t} = \rho_a \beta V_\infty + \dot{m}_{in} - \dot{m}_{e,s} \tag{26}$$

$$\rho_i L_F \frac{\partial B}{\partial t} = k_i \frac{\partial T}{\partial y} - k_w \frac{\partial \theta}{\partial y} \tag{27}$$

In equations (24)-(27) θ and T are the temperatures, k_w and k_i are the thermal conductivities, C_{pw} and C_{pi} are the specific heats and h and B are the thicknesses of water and ice layers, respectively. On the other hand, ρ_i and L_F denote the density of ice and the latent heat of solidification of water, respectively. Ice density is assumed to have different values for rime ice, ρ_r and glaze ice, ρ_g. The coordinate y is normal to the surface and ρ_a is the liquid water content.

In equation (26), $\rho_a \beta V_\infty$, $\dot{m}_{in}$ and $\dot{m}_{e,s}$ are impinging, runback and evaporating (or sublimating) water mass flow rates for a control volume, respectively. The boundary and initial conditions accompanying equations (24)-(27) are:

a) Ice is in perfect contact with the wing surface:

$$T(0,t) = T_s \tag{28}$$

The local adiabatic recovery temperature at the wall is calculated and imposed as a boundary condition [21] and the surface temperature is taken to be the recovery temperature [10]:

$$T_s = T_a + \frac{V_\infty^2 - U_e^2}{2C_p} \frac{1 + 0.2rM^2}{1 + 0.2M^2} \tag{29}$$

In the above expression, $M = V_\infty / a_\infty$, while the speed of sound is given by

$a_\infty = \sqrt{\gamma R T_a}$. Additionally, r is the adiabatic recovery factor ($r = Pr^{1/2}$ for laminar flow and $r = Pr^{1/3}$ for turbulent flow).

b) The temperature is continuous at the ice/water boundary and is equal to the freezing temperature, T_f :

$$T(B,t) = \theta(B,t) = T_f \tag{30}$$

c) At the air/water (glaze ice) or air/ice (rime ice) interface, heat flux is determined by convection, radiation, latent heat release, cooling by incoming droplets, heat brought in by runback water, evaporation or sublimation, aerodynamic heating and kinetic energy of incoming droplets.

d) Surface is initially clean:

$$B = h = 0, \ \ t = 0 \tag{31}$$

In the current approach, each panel constituting the geometry is also a control volume. The above equations are written for each panel and ice is assumed to grow perpendicularly to a panel.

Rime ice growth is expressed with an algebraic equation from the mass balance in equation (26), since water droplets freeze entirely on impact:

$$B(t) = \frac{\rho_a \beta V_\infty + \dot{m}_{in} - \dot{m}_{e,s}}{\rho_r} t \tag{32}$$

On the other hand, glaze ice thickness is obtained by integrating the ordinary differential equation obtained by combining mass and energy equations over time. The differential equation is:

$$\rho_g L_f \frac{\partial B}{\partial t} = \frac{k_i (T_f - T_s)}{B} + k_w \frac{(Q_c + Q_e + Q_d) - (Q_a + Q_k)}{k_w + h \frac{Q_c + Q_e + Q_d}{T_s - T_a}} - Q_{in} \tag{33}$$

In this expression, Q_c is heat flux by convection, Q_e is evaporation, Q_d is heat from incoming droplets, Q_a is aerodynamic heating, Q_k is kinetic energy of incoming droplets and Q_{ent} is the energy entering the control volume due to runback water. These terms are defined as:

$$Q_c = h_c (T_{sur} - T_a) \tag{34}$$

$$Q_e = \chi_e e_0 (T_{sur} - T_a) \tag{35}$$

where χ_e is the evaporation coefficient and e_0=27.03. Evaporation coefficient is expressed as [15]:

$$\chi_e = \frac{0.622 h_c L_E}{C_p P_t Le^{2/3}} \tag{36}$$

P_t is the total pressure of the airflow.

$$Q_d = \rho_a \beta V_\infty C_{pw}(T_{sur} - T_a) \tag{37}$$

where ε is the surface emissivity and σ_r is the Stefan-Boltzmann constant.

$$Q_a = \frac{r h_c {V_\infty}^2}{2C_p} \tag{38}$$

$$Q_k = \rho_a \beta V_\infty \frac{{V_\infty}^2}{2} \tag{39}$$

$$Q_{ent} = \dot{m}_{in} C_{pw}(T_f - T_{sur}) \tag{40}$$

where $\dot{m}_{in}$ is the mass flow rate of the incoming runback water.

It is assumed that, all of the unfrozen water passes to the neighboring downstream cell for the upper surface, while all water sheds for the lower surface. To calculate the glaze ice thickness, equation (33) is integrated numerically, using a Runge-Kutta-Fehlberg method.

3.5. MULTI-STEP CALCULATION APPROACH

In icing analysis, multi-step calculation approach is utilized. According to this approach, exposure time is divided into equal intervals. Abovementioned four steps for icing prediction are employed for each time interval. The geometry which is obtained at the end of an interval is taken as the new geometry in the next interval which is subject to icing.

Figure 17 illustrates an ice shape prediction obtained with 3 layers of computation. At the end of 1st step of computation, ice accumulated surface is considered as the new geometry and procedure is repeated where ice shape for 2nd layer is obtained. In the same manner, 3rd layer of computation is completed and the final ice shape is obtained.

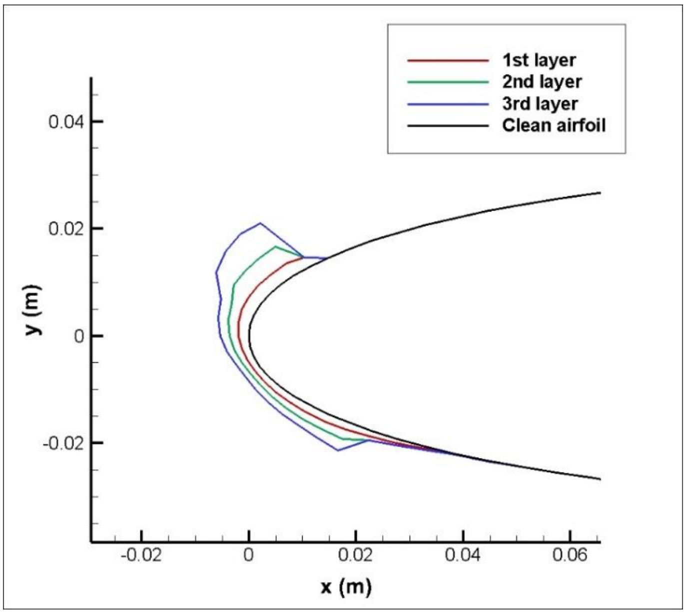

Figure 17: An example of ice shape prediction on an airfoil with 3-layer computation

This approach represents the transient problem in a quasi-steady fashion. The results obtained with multi-step calculation approach shows that increasing step number up to a threshold value improves the accuracy of the results especially for glaze ice conditions and for long exposure times.

3.6. ERROR ANALYSIS

In order to measure the success of the icing results obtained with the computational tool, validation studies are performed in which the current study results are compared with numerical and experimental literature data. The comparison can be done quantitatively or qualitatively. In qualitative manner, impingement limits on the surface, overall ice shape and ice thickness at certain locations can be examined and compared. On the other hand, a method is needed for quantitative approach. In the present study, methodology presented by Ogretim et al [16] are utilized for error computations.

According to this method, ice shape geometry is reduced to its Fourier coefficients with coordinate transformations. Through these transformations, the ice shape on the airfoil leading edge is modeled as a perturbation parabola. The perturbation geometry and the parabola itself pass through conformal mapping. At the end, airfoil surface becomes a straight line and the ice geometry becomes a perturbation to this straight line in the transformed plane. Transformation procedure is outlined as [16]:

The original coordinates in the x-y plane is scaled based on leading edge radius (LER) to coincide with the parabola leading edge.

$$x' = \frac{x/c}{LER/c} - 0.5 \tag{41}$$

$$y' = \frac{y/c}{LER/c} \tag{42}$$

where c denotes the chord length of the airfoil. Ice shape is considered as perturbations to the parabola leading edge. The transformation from the scaled plane $(x' - y')$ to $(\xi' - \eta')$ plane with conformal mapping [16] is accomplished by:

$$x' = ({\xi'}^2 - {\eta'}^2)/2 \tag{43}$$

$$y' = \xi'\eta' \tag{44}$$

The roughness geometry (transformed ice shape) from the base surface (clean airfoil surface) is separated with Prandtl transposition [16]:

$$\xi' = \xi \tag{45}$$

$$\eta' = \eta + f(\xi) \tag{46}$$

After these transformations, ice shape is obtained as in Figure 18 in the transformed plane as a perturbation.

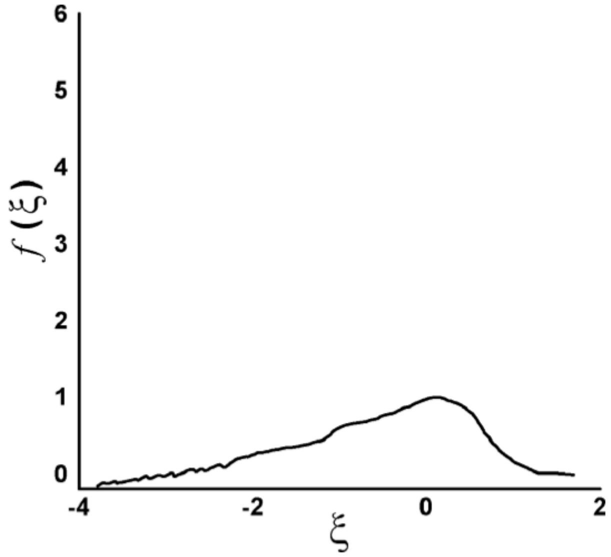

Figure 18: Ice shape as perturbation in the transformed plane [16]

For error analysis, ice shapes obtained with experiment and prediction are transformed and perturbation curves are plotted in $(\xi - f(\xi))$ plane as in Figure 19. An area weighted relative error is computed with the following relation [16]:

$$Error = \frac{\sum_{i=1}^{N} |f_{e_i} - f_{p_i}| \Delta\xi_i}{\sum_{i=1}^{N} |f_{e_i}| \Delta\xi_i} \tag{47}$$

where subscript e denotes the experimental ice thickness and the subscript p denotes the predicted ice thickness and N is the total number of data points. Area weighted true relative error is equal to the ratio of the area between prediction and the experiment to the experimental ice area. In this error calculation, ice shape area is not compared but the ice mass formed on the surface is considered.

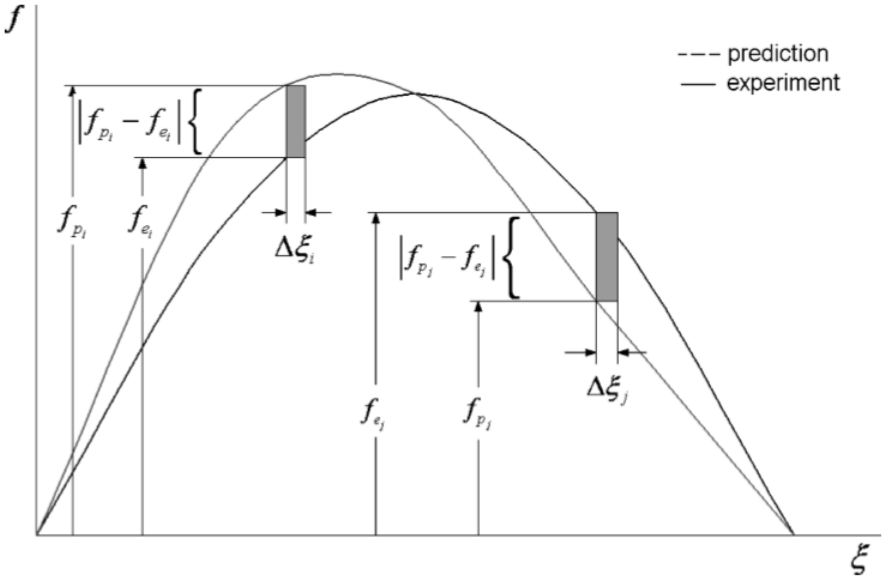

Figure 19: Geometrical depiction for the cumulative error [16]

CHAPTER 4

SUPERCOOLED LARGE DROPLETS (SLD)

FAA and EASA have defined meteorological conditions for an aircraft to be tested against in order to show that it can fly safely in the specified icing conditions. These icing conditions are valid for supercooled droplets with diameters between 15-50 μm. On the other hand, there have been incidents and accidents in which droplet sizes are much larger than 50 μm, up to 1000-2000 μm [33]. Therefore, a wide range of droplet sizes and icing conditions must be considered in icing simulations.

Supercooled Large Droplets (SLD) differ from supercooled droplets with having a non-spherical shape and some physical phenomena such as droplet splash and droplet break-up. Hence, icing simulations must be performed by taking these effects into account. How these differences are included in the calculations of the current study are explained in the following.

4.1. Drag Coefficient Calculation

SLD may be in non-spherical shapes which is directly effective on drag calculation. Drag is calculated with equation 7 in Chapter 3, whereas drag coefficient C_D differs for SLD which is obtained with the model suggested by Clift, Grace and Weber, which takes non-spherical shapes of large droplets into account [7]:

$$C_D = e\, C_{D,disk} + (1-e) C_{D,sphere} \tag{48}$$

According to this model, the effective droplet drag coefficient is obtained by interpolation between a disk and a sphere, where the eccentricity e, depends on the Weber number.

$$e = 1 - \frac{1}{(1 + 0.007\sqrt{We})^6} \tag{49}$$

where Weber number is defined as:

$$We = \frac{\rho V_{rel}^2 d_p}{\sigma_w} \tag{50}$$

ρ denotes air density, V_{rel} is relative velocity, d_p is particle diameter and σ_w denotes surface tension of water. Weber number describes the ratio between deforming inertial forces and stabilizing cohesive forces for liquids flowing through a fluid medium. As velocity and droplet size increases or surface tension decreases, Weber number increases which means that droplet will deform more easily.

The drag coefficient of an oblate disk as a function of the droplet Reynolds number is given by the following law [7]:

$$Re \leq 0.01, \qquad C_D = \frac{64}{\pi\, Re}\left(1 + \frac{Re}{2\pi}\right) \tag{51}$$

$$0.01 < Re \leq 1.5, \qquad C_D = \frac{64}{\pi\, Re}(1 + 10^x) \tag{52}$$

$$1.5 < Re \leq 133, \qquad C_D = \frac{64}{\pi\, Re}(1 + 0.138 Re^{0.792}) \tag{53}$$

$$Re > 133, \qquad C_D = 1.17 \tag{54}$$

with $x = -0.883 + 0.906 log_{10} Re - 0.025 (log_{10} Re)^2$.

The drag coefficient of a sphere is given as follows with $w = log_{10}Re$:

$$Re \leq 0.01, \qquad C_D = \frac{9}{2} + \frac{24}{Re} \tag{55}$$

$$0.01 < Re \leq 20, \qquad C_D = \frac{24}{Re}\left[1 + 0.1315Re^{(0.82-0.05w)}\right] \tag{56}$$

$$20 < Re \leq 260, \qquad C_D = \frac{24}{Re}\left[1 + 0.1935Re^{0.6305}\right] \tag{57}$$

$$260 < Re \leq 1500, \qquad log_{10}C_D = 1.6435 - 1.1242w + 0.1558w^2 \tag{58}$$

$$1500 < Re \leq 12000 \qquad \begin{aligned} log_{10}C_D = -2.4571 + 2.5558w - 0.9295w^2 \\ + 0.1049w^3 \end{aligned} \tag{59}$$

$$12000 < Re \leq 44000 \qquad log_{10}C_D = -1.9181 + 0.637w - 0.0636w^2 \tag{60}$$

$$44000 < Re \leq 338000 \qquad log_{10}C_D = -4.339 + 1.5809w - 0.1546w^2 \tag{61}$$

$$338000 < Re \leq 400000 \qquad C_D = 29.78 - 5.3w \tag{62}$$

$$400000 < Re \leq 10^6 \qquad C_D = 0.1w - 0.49 \tag{63}$$

$$10^6 < Re \qquad C_D = 0.19 - \frac{80000}{Re} \tag{64}$$

4.2. Droplet Break-up

If a supercooled large droplet has a high enough velocity, it can break up because of the shear forces which overcome surface tension that tries to keep it intact. Droplet break-up occurs when Weber number of the droplet exceeds critical Weber number. Although it varies from model to model, critical Weber number is accepted about 10-20 according to literature. In this thesis, threshold Weber number is taken as 12 which is an acceptable value. Figure 20 depicts Weber number variation of 1000 μm droplets moving towards an airfoil. It is noticed that drops will break up before reaching the airfoil according to the Weber number criteria. The break-up criteria is reached by the first green line [33].

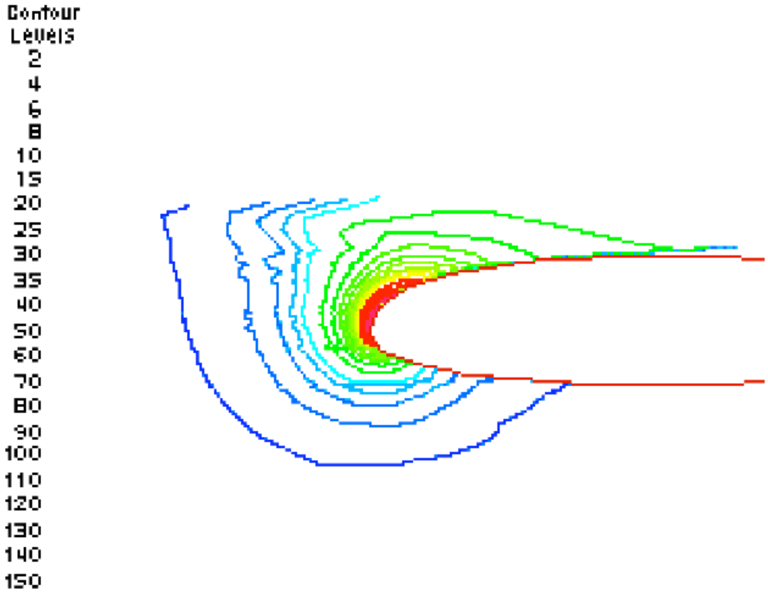

Figure 20: Weber Number on a 1000 micron drop [33]

Trajectory calculation is continued after break-up with the secondary droplet until it impacts on the surface. Diameter of the secondary droplet is found with:

$$d_s = 6.2\left(\frac{\rho_w}{\rho_{air}}\right)^{0.25} {Re_w}^{-0.5} d_p \tag{65}$$

$$Re_w = \frac{\rho_w V_{rel} d_p}{\mu_w} \tag{66}$$

ρ_w and ρ_{air} denotes water and air density respectively, Re_w Reynolds number of water and d_p droplet diameter before break-up.

4.3. Droplet Splashing

All of the droplets do not impinge on the surface, i.e. some of them splash. Droplet splashing has a first order effect on ice accumulation for SLD [32]. In order to model droplet splashing, a detailed physical model is required by solving Navier-Stokes equations for each droplet impact with Volume of Fluid (VOF) approach which is described in literature [12], [29]. However, an empirical approach is utilized in the current study in order to avoid costly computations.

After a droplet impacts the surface, part of its mass will impinge on the surface, while the remaining mass will bounce and reimpinge downstream [31]. The bouncing and reimpinging water is treated as runback water in this study. Cossali et al [8] present their results in terms of the non-dimensional group:

$$K = \left(\frac{{\rho_w}^3 {d_p}^3 {V_n}^5}{{\sigma_w}^2 \mu_w} \right)^{0.25} = Oh^{-2/5}\, We_n \tag{67}$$

In equation 67, K denotes Mundo splashing factor, Weber number is based on normal component of droplet velocity, V_n at impact. Ohnesorge number, Oh, is defined as:

$$Oh = \frac{\mu_w}{\sqrt{\rho_w d_p \sigma_w}} \tag{68}$$

For splash threshold and properties of the splashed droplet, splashing factor is modified as:

$$K_m = \sqrt{K} f^{-3/8} \tag{69}$$

where f is a non-dimensional droplet frequency defined as:

$$f = \frac{3}{2}\left(\frac{\rho_a}{\rho_w}\right)^{1/3} \tag{70}$$

Splashing criteria is K_m>17 according to [33] and splashed mass and secondary droplet size are defined respectively as:

$$\frac{m_s}{m_o} = 0.2\left[1 - e^{-0.85(K_m-17)}\right] \tag{71}$$

$$\frac{d_s}{d_p} = 8.72e^{-0.0281K} \tag{72}$$

m_o is the incident mass and m_s is the splashed mass in equation (71).

CHAPTER 5

VALIDATION STUDIES ON AIRFOIL GEOMETRIES

Although the subject of the thesis is about icing simulations on engine intakes, validation studies on icing simulations for airfoils are presented as well in this chapter. The reason behind this is to demonstrate that the computational tool is capable of simulating ice accretion accurately on airfoil geometries for a wide range of icing conditions which would be modified for engine intakes later. Furthermore, there are a great number of experimental and numerical data available in literature for icing simulations on different airfoil geometries, which is not the case for engine intakes as mentioned before. When geometric similarity in engine intake lip and airfoils is considered, validation studies on airfoil icing simulations brought great advantage during developing of the computational tool for engine intakes.

5.1. NACA0012 Validation Results

Two validation studies are performed for NACA0012 airfoil profile which is shown in Figure 21. In the first one, ice shape prediction results are obtained and compared with numerical data obtained by DRA (Defence Research Agency), NASA (National Aeronautics and Space Administration) and ONERA (Office National D’Etudes et des Recherches Aerospatiales) and experimental data presented in [35]. In the second part of NACA0012 validation studies, ice shape results are compared for different icing conditions and compared with numerical data obtained with LEWICE 2.0 and 3.0 (software developed by NASA) and experimental data which are provided in [32].

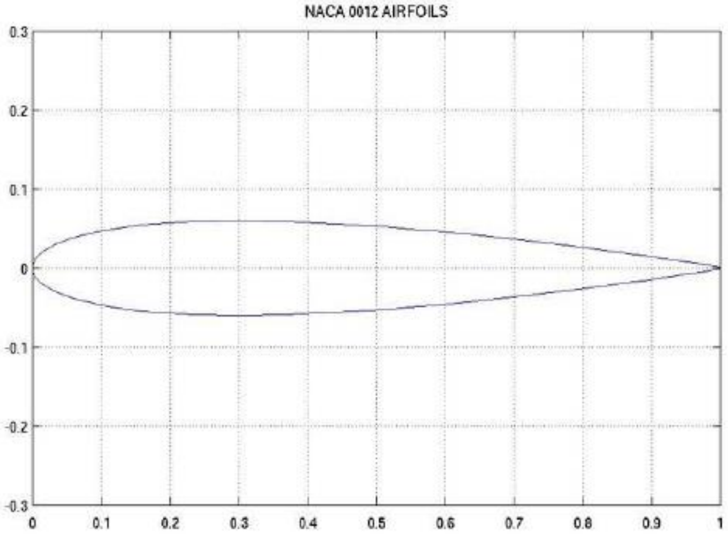

Figure 21: NACA0012 airfoil

5.1.1. NACA0012 Validation Study-Part I

Icing conditions to be tested are given in Table 1 for NACA0012 airfoil profile. The chord length is 0.53 meters, median volumetric diameter is 20 μm and relative humidity is 100% for all test cases. Velocity, static temperature, pressure, liquid water content and exposure time are varying in each test condition.

Table 1: Icing conditions for NACA0012 airfoil profile [35]

Test no	Angle of attack (°)	Velocity (m/s)	T_{static} (°C)	Pressure (kPa)	LWC (g/m^3)	Exposure time (s)
27	4	58.1	-27.8	95.61	1.3	480
32	4	58.1	-2.8	95.61	1.3	480
33	4	93.8	-30.5	92.06	1.05	372
36	4	93.8	-6.6	92.06	1.05	372

Ice shape results obtained for these icing conditions are compared with experimental and numerical data obtained by DRA, ONERA and NASA. While comparing with other numerical results, one should remember that reference numerical data were obtained in 1997 in the circumstances of that time.

- **Test-27**

Figure 22 shows the parametric study for number of computational steps for icing prediction of Test 27 icing condition. Since angle of attack is 4°, ice accumulates mostly on the lower half of the airfoil leading edge. The closest ice shape to experimental data is obtained with 2 layers of calculation, which captures overall ice thickness at the leading edge quite well. Although impingement limits are slightly underestimated, ice mass could be said to be predicted successfully.

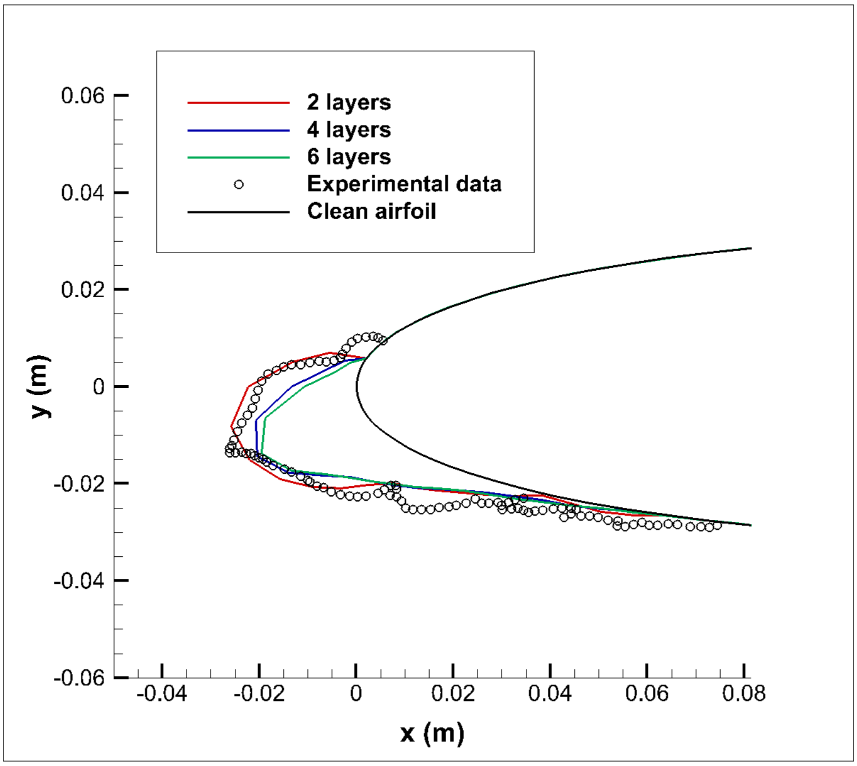

Figure 22: Ice shape predictions obtained with different numbers of computation layers for Test-27

In Figure 23, current study ice shape result obtained with 2 layers of calculation is compared with numerical data presented by ONERA, NASA, DRA and experimental data in [35]. DRA overestimates the ice accreted on the surface while ONERA and NASA underestimate the ice mass when compared to experimental data. NASA predicts horn-like ice shape, which is a characteristics of glaze ice although the icing condition corresponds to rime ice. The current study ice shape result can be said to be in better agreement with experimental data than the other numerical results.

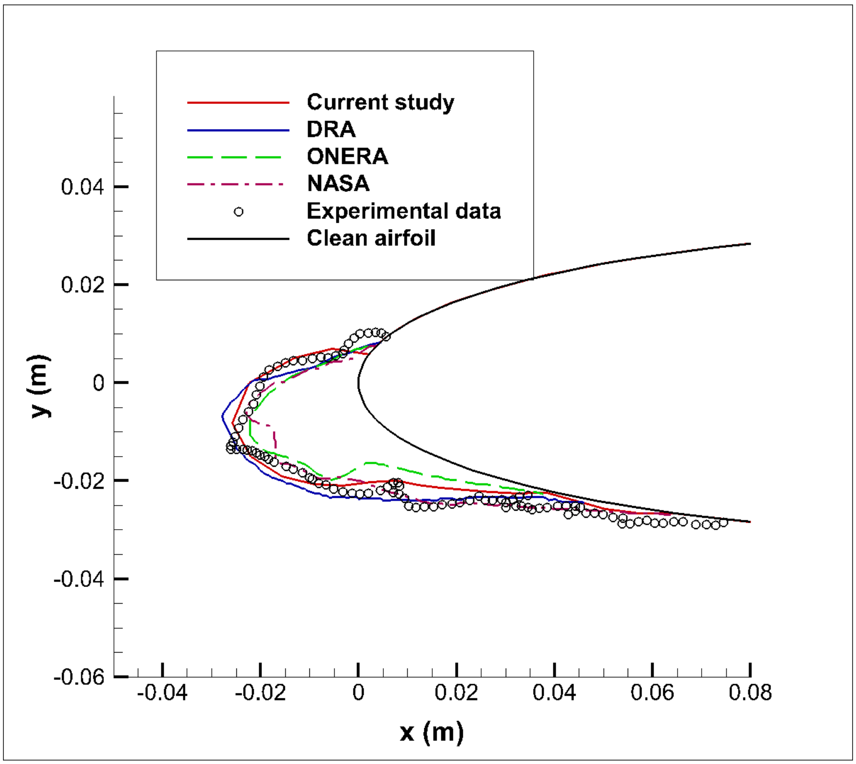

Figure 23: Ice shape comparison of current study, reference numerical and experimental data for Test-27

- **Test-32**

Figure 24 depicts the ice shapes obtained with 2, 4 and 6 layers of calculation for Test 32 condition. Due to non-zero angle of attack, ice accumulates on the lower half of the geometry. The best prediction is obtained with 6 layers of calculation. Over all ice shape and upper impingement limit is captured quite well when compared with experimental data although lower impingement limit is underestimated. Increasing number of calculation layers obviously improves ice shape prediction, which is expected considering glaze ice condition.

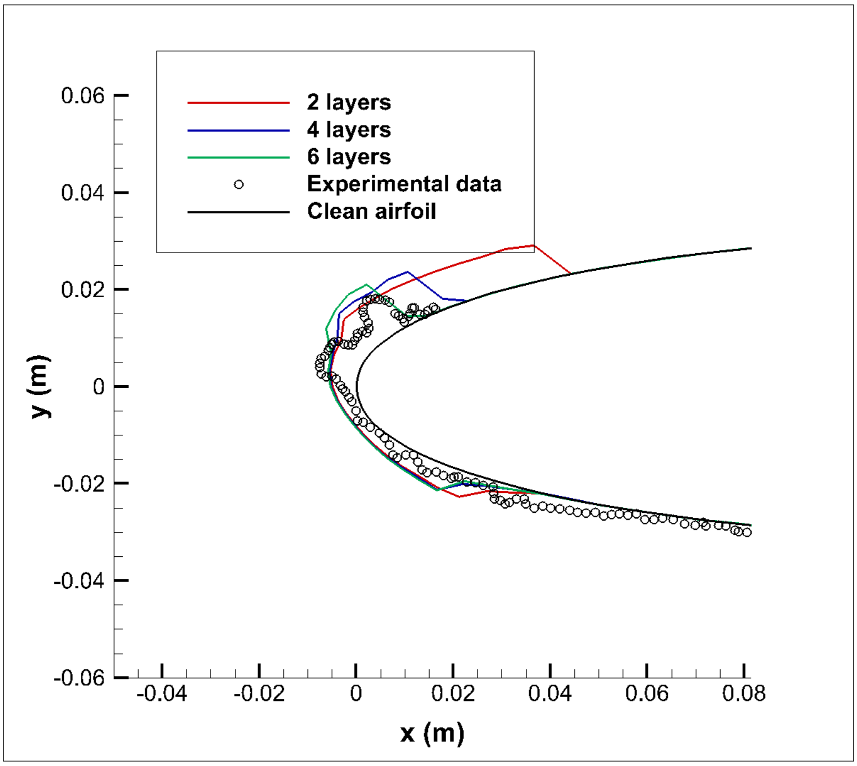

Figure 24: Ice shape predictions obtained with different numbers of computation layers for Test-32

Current study ice shape result with 6 layers of calculation is compared with experimental and numerical literature data in Figure 25. It is clearly seen that current study predicts ice shape to be formed on the airfoil surface much better in terms of overall shape and impingement limit on the upper surface.

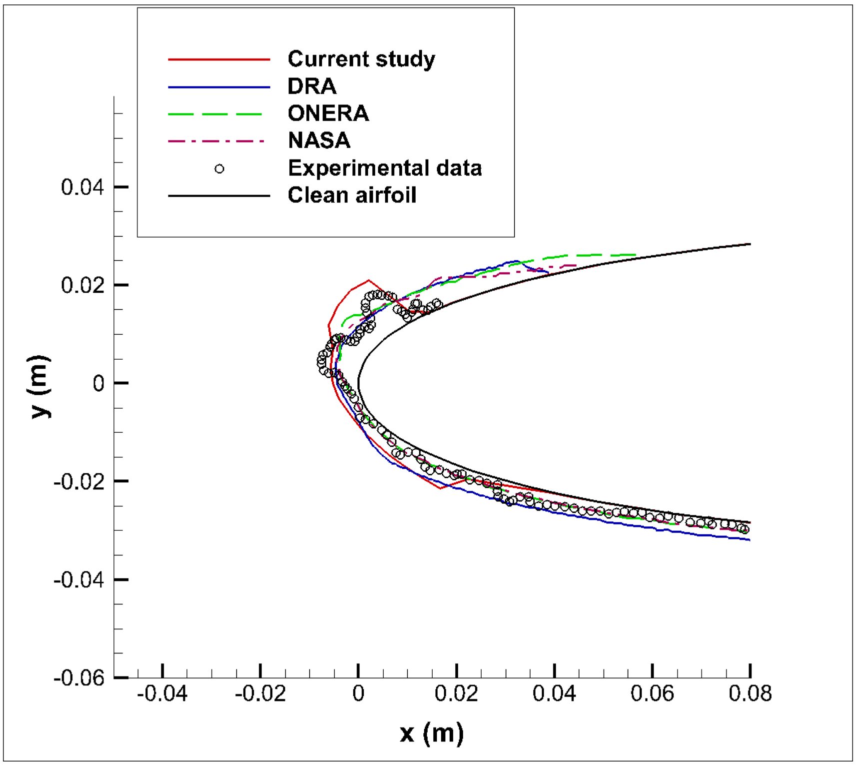

Figure 25: Ice shape comparison of current study, reference numerical and experimental data for Test-32

- **Test-33**

Test 33 is also a rime ice condition like Test 27 with temperature of -30.5°C. Increasing number of calculation steps does not enhance the ice shape prediction since it is rime ice condition. The best ice shape result is achieved with 2 layers of calculation. Ice thickness is predicted very close to experimental data although the impingement limits are slightly off.

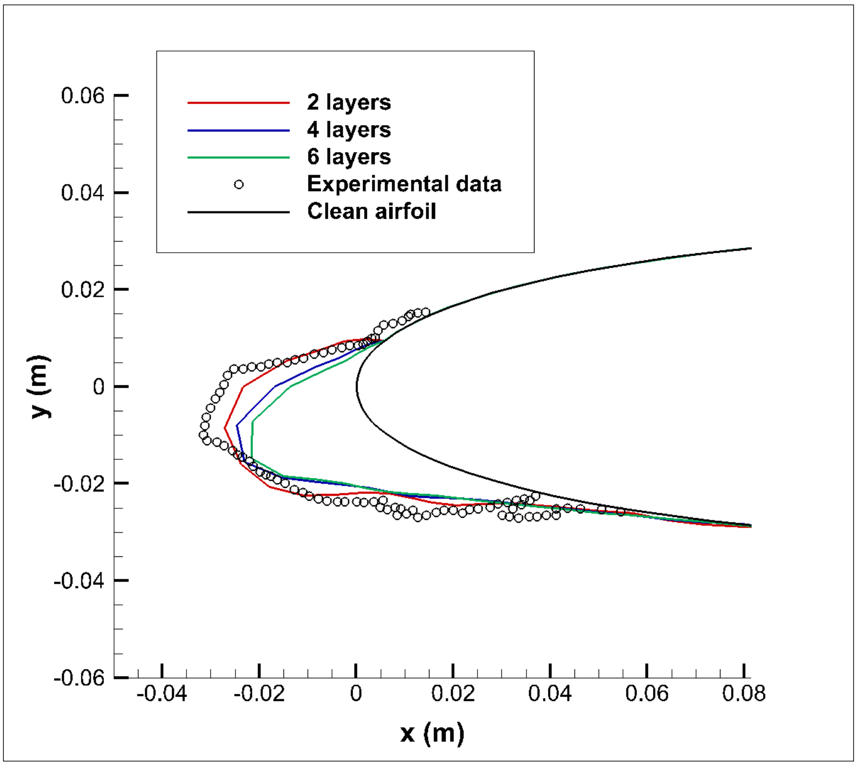

Figure 26: Ice shape predictions obtained with different numbers of computation layers for Test-33

As seen in Figure 27, NASA and ONERA estimates a smaller ice mass whereas DRA and current computational tool predicts a very close ice shape to experimental data. Although they do not capture the sharp edge as in experimental result, the predicted ice shape could be said to be in well agreement.

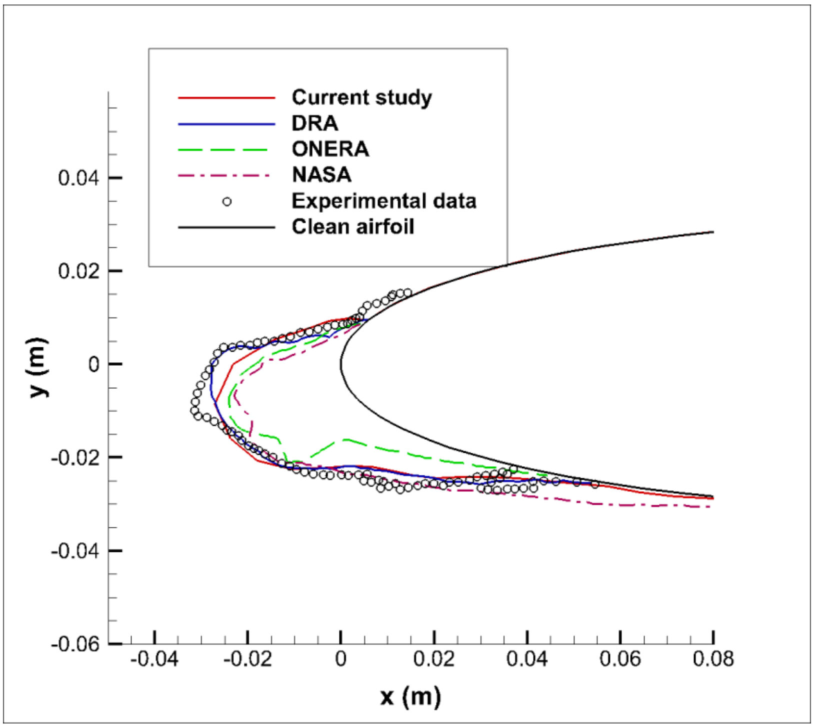

Figure 27: Ice shape comparison of current study, reference numerical and experimental data for Test-33

- **Test-36**

Test-36 is a glaze ice condition with temperature of -6.6°C. As seen in Figure 28, 6 layers of computation yields the best ice shape prediction, which captures the sharp edge on the top and impingement limits.

Figure 29 shows that all computational tools predict similar ice shapes for the given icing condition. DRA could be said to estimate the best ice shape when compared to experimental data. Current study and ONERA results are similar and overestimate the ice mass accumulated on the airfoil surface. NASA obtains an ice accumulation close to DRA results although the lower impingement limit is not predicted well.

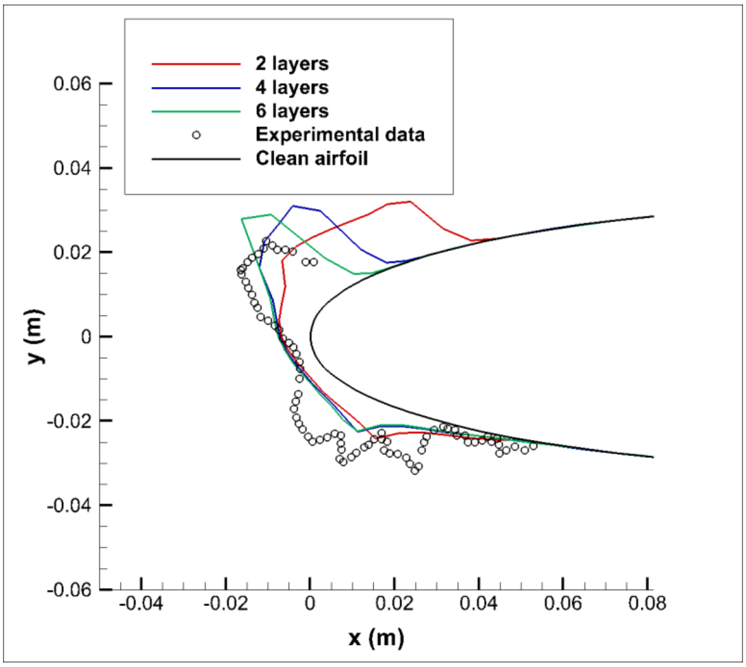

Figure 28: Ice shape predictions obtained with different numbers of computation layers for Test-36

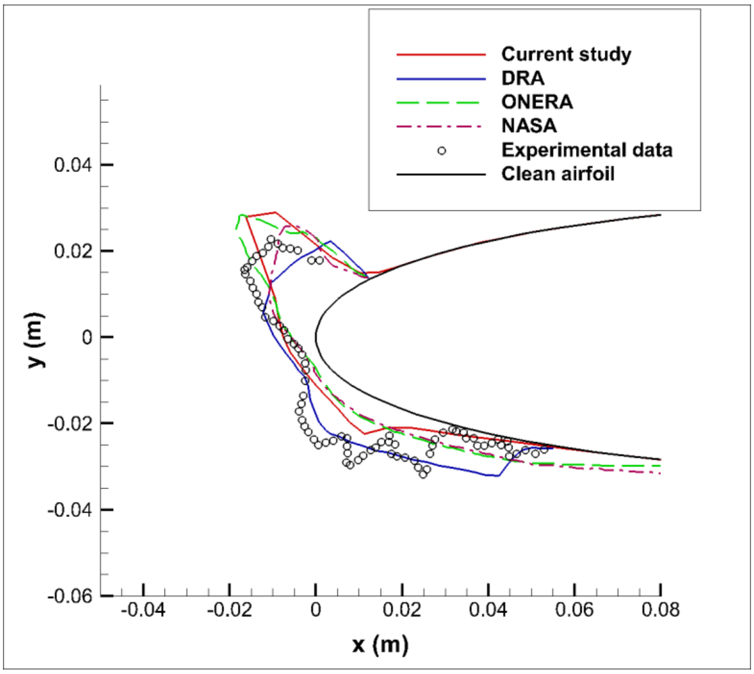

Figure 29: Ice shape comparison of current study, reference numerical and experimental data for Test-36

In this validation study, it is concluded that increasing number of calculation steps enhances ice shape prediction success for glaze ice conditions. For rime ice condition, lower step number gives better ice shape results. Overall ice shapes obtained can be said to be in agreement with experimental results. Estimation of the impingement limits can be improved by increasing the number of panels on the geometry. 201 panels are utilized during the computations in the current study.

Error analysis is performed with area weighted true relative error method which is explained in Section 3.6. Table 2 shows errors in percentage for the test cases. It is noticed that ice mass that accumulates on the airfoil leading edge is predicted with an error less than 5% except for Test-27. For this test case, upper and impingement limits are missed in addition to smaller ice thickness on the lower surface when compared to experimental data. Error of 12.4% is caused by these poor predictions.

Table 2: Errors between ice predictions obtained with experiment and developed tool

Test case	**Error %**
Test-27	12.4
Test-32	4.7
Test-33	3.0
Test-36	1.9

5.1.2. NACA0012 Validation Study-Part II

In this part of the thesis, further validation study on NACA0012 airfoil geometry is performed. Icing conditions that are tested are listed in Table 3. It is seen that there are three icing conditions for varying droplet sizes (MVD), liquid water content, velocity and exposure times. Total temperature values are quite close in all cases and correspond to rime ice conditions. The results are compared with the numerical data reported in the literature obtained with LEWICE 2.0 and LEWICE 3.0 (software developed by NASA) and experimental data which are presented by Wright and Potapzcuk [32]. LEWICE 3.0 differs from LEWICE 2.0 in the procedure for interfacing with Naviér-Stokes solvers which has been enhanced and having a model for supercooled large droplet (SLD) phenomena [36].

Table 3: Test conditions for icing predictions on NACA0012

	MVD (µm)	**LWC (g/m^3)**	**Velocity (m/s)**	**T_{tot} (ºC)**	**Exposure time (s)**
Test 1-22	40	1.02	77	-19.3	576
Test 1-1	70	0.91	51	-19.6	804
Test 1-4	160	1.5	52	-19.5	300

In the ice shape prediction analyses, multi-step calculation approach is applied. Moreover, SLD effects are investigated by including droplet breakup, splash and droplet drag coefficient. The results obtained by including SLD effects in the calculations are demonstrated as “SLD: on” and by excluding these effects are shown as “SLD: off” in the figures. Ice shape prediction results are presented for the test cases given in Table 3.

- **Test 1-22**

Ice shape predictions are obtained for varying number of calculations with SLD effects included and excluded respectively as shown in Figure 30 and Figure 31. Although increasing number of calculation do not improve the ice shape results much, 12 layers of computational step yield slightly closer results to experimental data presented in [32] for both “SLD: on” and “SLD: off” cases.

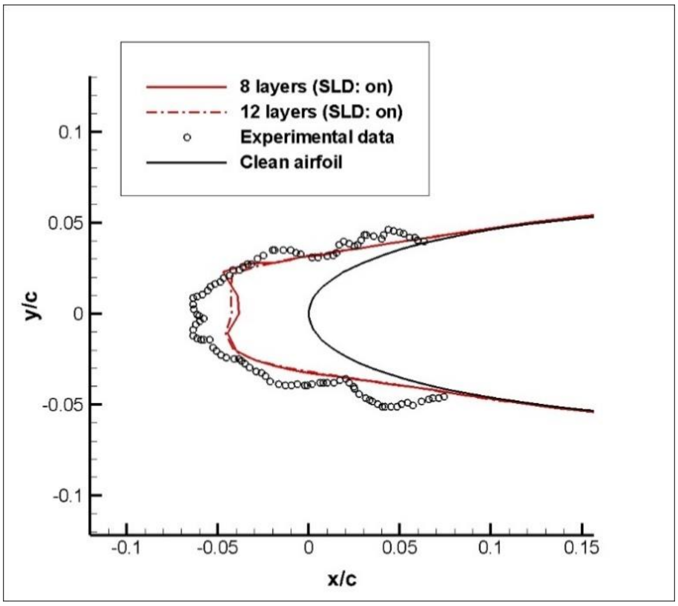

Figure 30: Ice shape predictions with different layers of calculation for Test 1-22 (SLD: on)

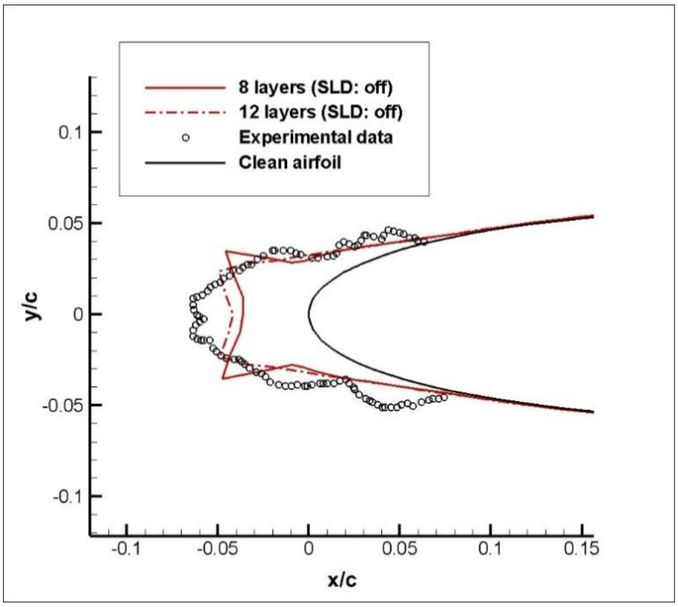

Figure 31: Ice shape predictions with different computational step numbers for Test 1-22 (SLD: off)

Having the best ice shape prediction with 12 layers of calculation, the effect of including SLD characteristics in the calculations are examined for the same computational step number as shown in Figure 32. Switching on SLD effects do not enhance the results significantly obtained for ice shape which is expected since MVD for Test 1-22 is 40 μm which is not considered as an SLD case. Although the results with and without SLD effects seem very close to each other, "SLD: off" case could be said to be better considering the symmetric horn-like shape as in experimental data.

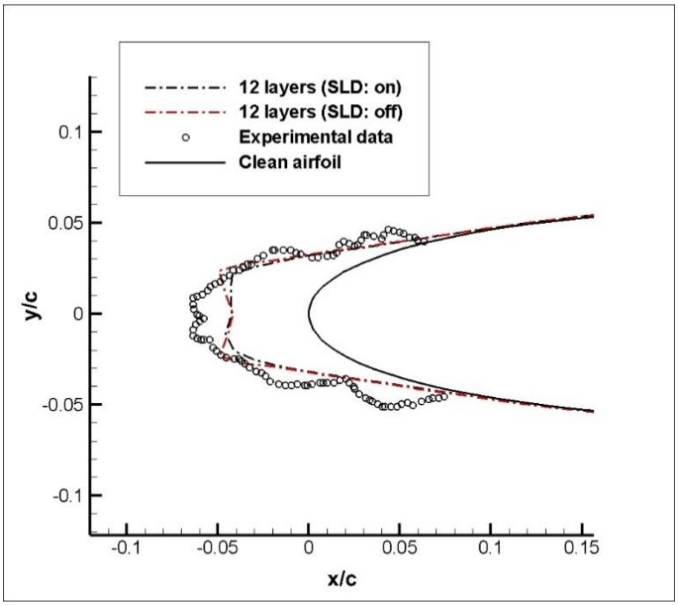

Figure 32: SLD effect on ice shape prediction for Test 1-22 (12 layers)

The best ice shape prediction obtained is without SLD effects and 12 layers of calculation as shown Figure 33. Current study result is compared with numerical and experimental data presented in [32] as in Figure 33. Although LEWICE 2.0 predicts the horn shape well, it overestimates the ice thickness. LEWICE 3.0 predicts a smaller ice mass and smoother ice shape. Current study captures the horn shape better than the other numerical studies, although it predicts the ice thickness slightly thinner than the experimental result.

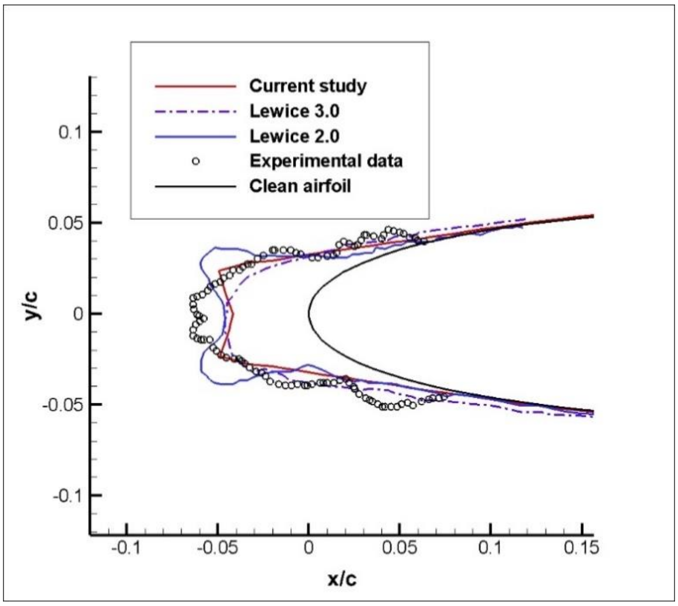

Figure 33: Comparison of current study result (12 layers, SLD: off) with reference numerical and experimental data for Test 1-22

- **Test 1-1**

Test 1-1 icing condition is for droplet size with MVD of 70 μm and exposure time is 804 s. Ice shape predictions obtained with 6 and 12 computational steps by including and excluding SLD effects are shown in Figure 34 and Figure 35, respectively. It is observed that increasing number of computational steps do not enhance the ice shape prediction when compared with experimental data for “SLD: on” results which is reasonable since Test 1-1 condition with MVD of 70 μm is not a truly SLD case. On the other hand, 12 layers of calculation yields a closer ice shape to experimental result for “SLD: off” case despite the slight improvement in the ice shape when compared with 6 layers of computation.

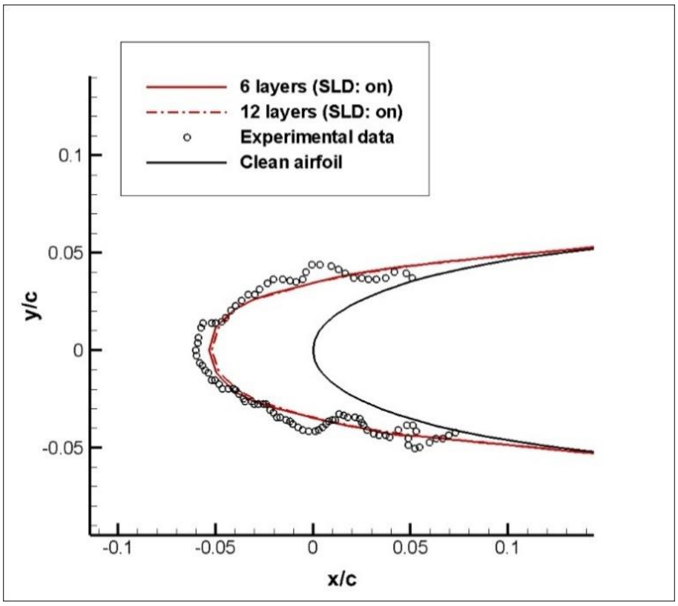

Figure 34: Ice shape predictions with different computational step numbers for Test 1-1 (SLD: on)

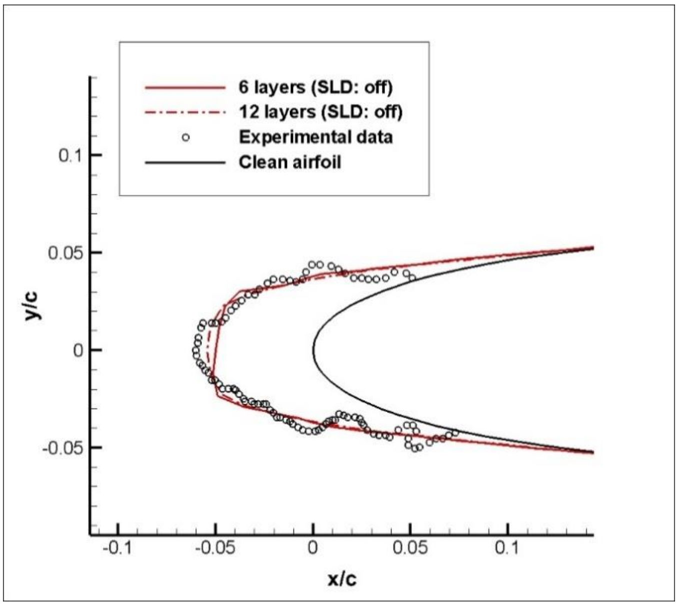

Figure 35: Ice shape predictions with different computational step numbers for Test 1-1 (SLD: off)

The effect of including and excluding SLD effects like droplet break-up and splash on ice shape prediction for Test 1-1 is given in Figure 36 for 12 layers of computational step. Ice mass obtained with “SLD: on” option is less than “SLD: off” case. This situation is expected since including droplet break-up and splash yields less ice mass accumulation on the surface. It is obvious that SLD: off case captures the ice thickness slightly better than SLD: on case and is very close to experimental data.

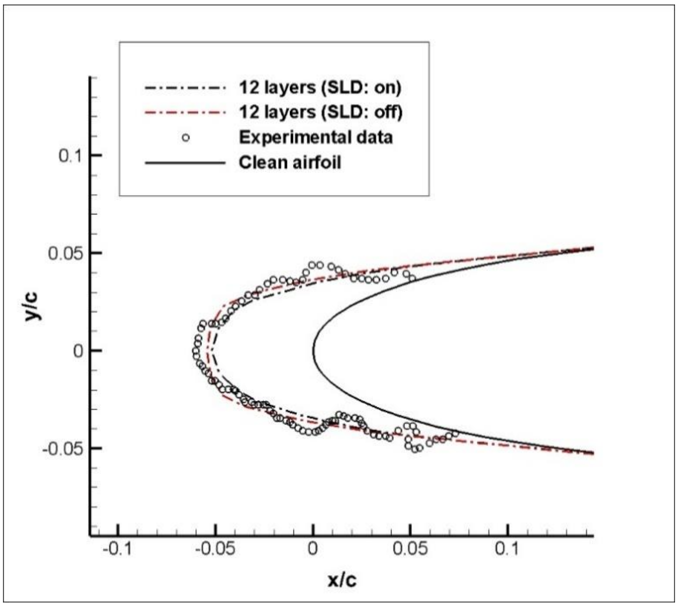

Figure 36: SLD effect on ice shape prediction for Test 1-1 (12 layers of calculation)

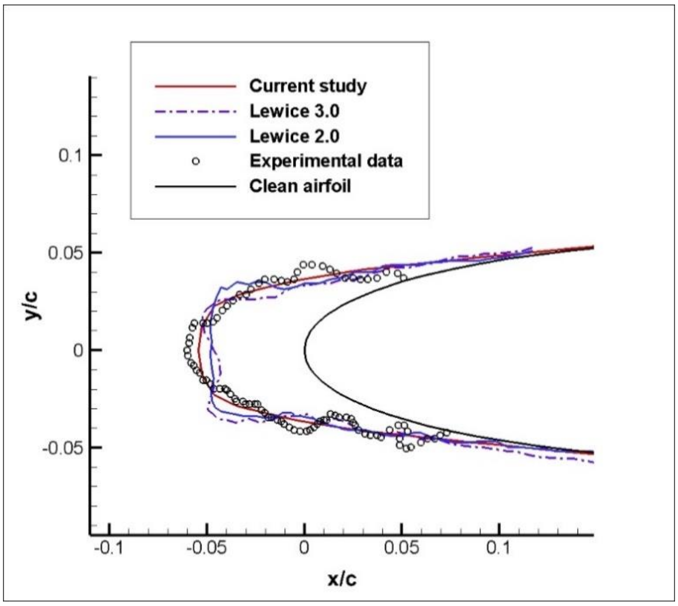

Figure 37: Comparison of current study result (12 layers, SLD: off) with reference numerical and experimental data for Test 1-1

In the light of the parametric studies on number of computational step and SLD effects, the closest ice shape result to the experimental data is 12 computational steps without SLD effects. This result is compared with experimental and numerical data in Figure 37. LEWICE 2.0 and 3.0 results are very similar to each other although LEWICE 3.0 predicts an ice shape with horns. It overestimates the ice thickness in normal direction. The current study ice shape result seems closest to the experimental data considering ice thickness and shape.

- **Test 1-4**

Test 1-4 differs from other two icing conditions with MVD of 160 μm which corresponds to SLD. Different numbers of computational steps are tested with and without inclusion of SLD effects which are presented in Figure 38 and Figure 39.

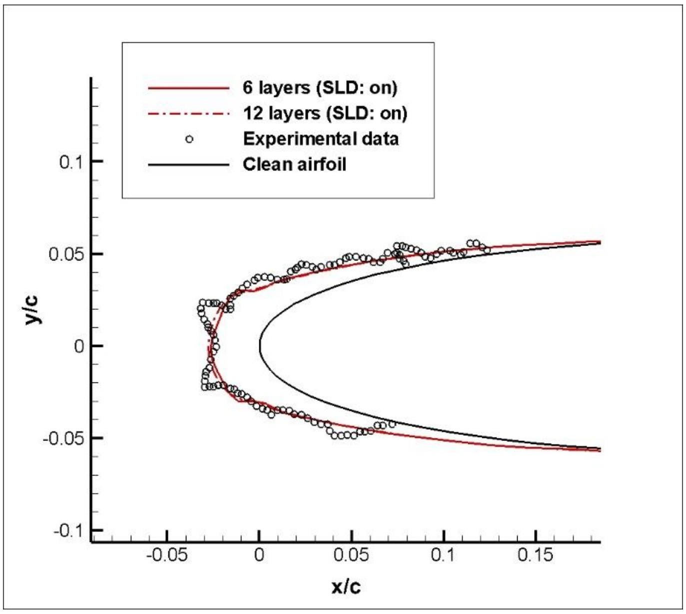

Figure 38: Ice shape predictions with different computational step numbers for Test 1-4 (SLD: on)

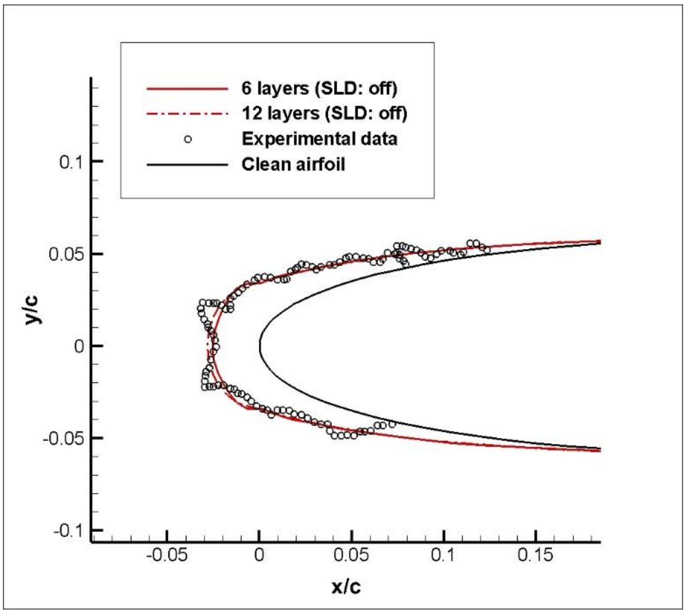

Figure 39: Ice shape predictions with different computational step numbers for Test 1-4 (SLD: off)

For both predictions, it is seen that increasing number of computational steps does not improve ice shape results. Although the ice thickness is captured very well, impingement limits are estimated slightly broader. Since increasing number of computational steps leads to high CPU time, 6 layers of calculation is chosen for the ice shape prediction in Test 1-4. When inclusion of SLD effects into the calculations are considered as in Figure 40, there is only a minor superiority of "SLD: on" case in the region around x/c=0.

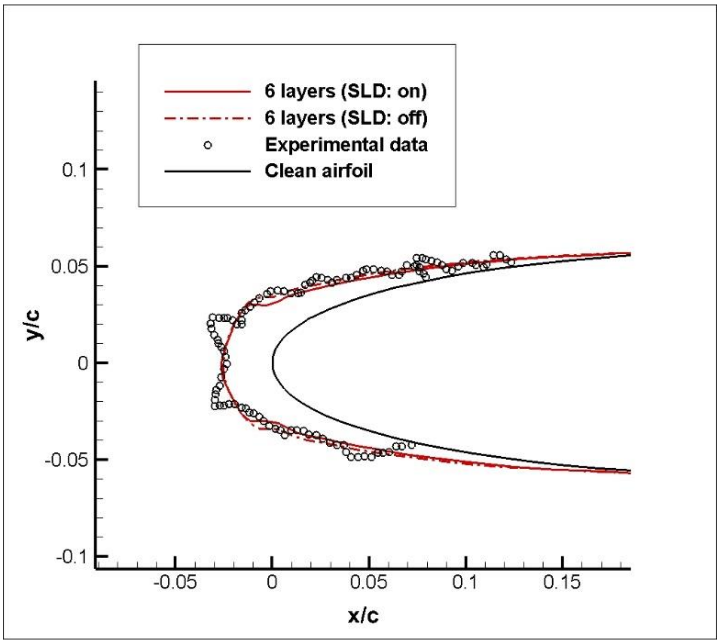

Figure 40: SLD effect on ice shape prediction for Test 1-4

Figure 41 depicts the comparison of current study ice shape results with numerical and experimental results. LEWICE 2.0 obtains a thicker ice mass when compared with the others. Current study and LEWICE 3.0 results are quite similar to each other which predict the ice thickness successfully, but both miss the small horn shape observed in the experiment close to the leading edge.

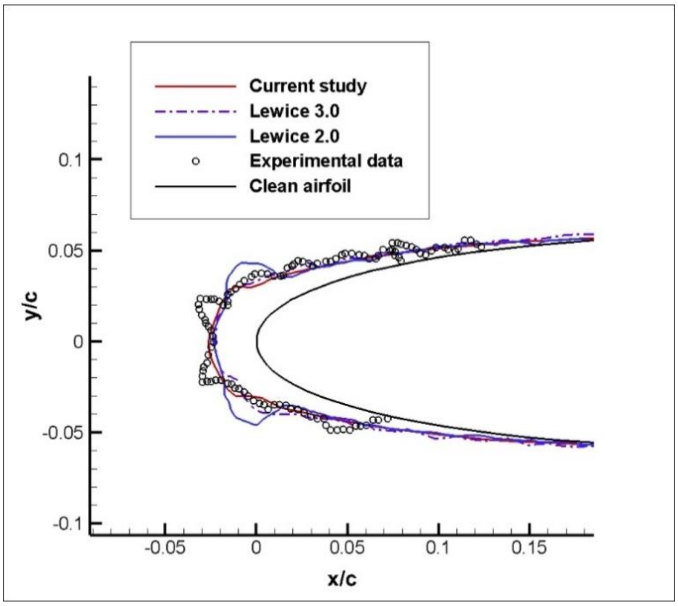

Figure 41: Comparison of current study result (6 layers, SLD: on) with reference numerical and experimental data for Test 1-4

In the validation study of NACA0012 airfoil profile, it is deduced that the computational tool can be said to apply SLD effects if needed in the corresponding icing conditions. Moreover, time interval of 45-70 seconds for each layer of calculation gives better ice shape results, which is observed in parametric studies in multi-step calculation for different exposure time values.

The results in this section confirm that the current computational tool successfully predicts the ice shapes for the given test cases, which are rime or rime-like due to the low temperature, in spite of the relatively high LWC. Inclusion of SLD effects only slightly improves the results when droplet sizes are equal to or greater than 70 µm.

5.2. MS317 Airfoil Validation Results

Collection efficiencies on MS317 airfoil profile shown in Figure 42 are presented in this validation study. The results are compared with both experimental and numerical data presented in [32]. The effect of droplet size and angle of attack on collection efficiency is investigated. Chord length of the airfoil is 0.915 m, liquid water content is 0.5 g/m^3 and velocity is 78 m/s in all test conditions.

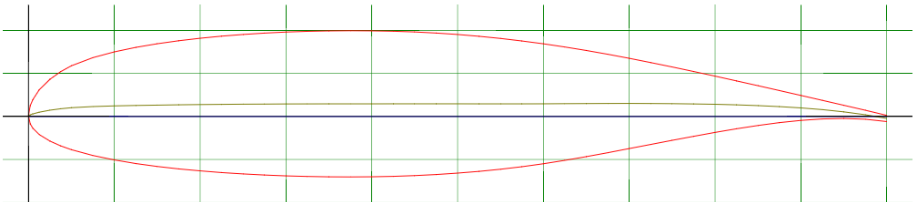

Figure 42: MS317 airfoil

Collection efficiencies on MS317 for MVD of 21μm, 92 μm and 236 μm and angle of attack values of 0^o and 8^o for each droplet size are calculated. The effect of including SLD effects such as break-up and splash are investigated in the analyses as well. In the results, positive values of s/c represent upper half surface of the airfoil whereas negative values of s/c represent lower half surface of the airfoil.

Figure 43 and Figure 44 depict collection efficiencies on MS317 for MVD = 21 μm and angle of attack values of 0^o and 8^o, respectively. Maximum collection efficiency occurs at the leading edge for zero angle of attack case while it occurs on the lower surface of the airfoil for 8^o case. Majority of the ice is accumulated on the lower surface as well. “SLD: on” results are poorer compared to “SLD: off” results which is reasonable since MVD=21 μm is not an SLD case and including SLD effects do not improve results but diverge from the experimental results.

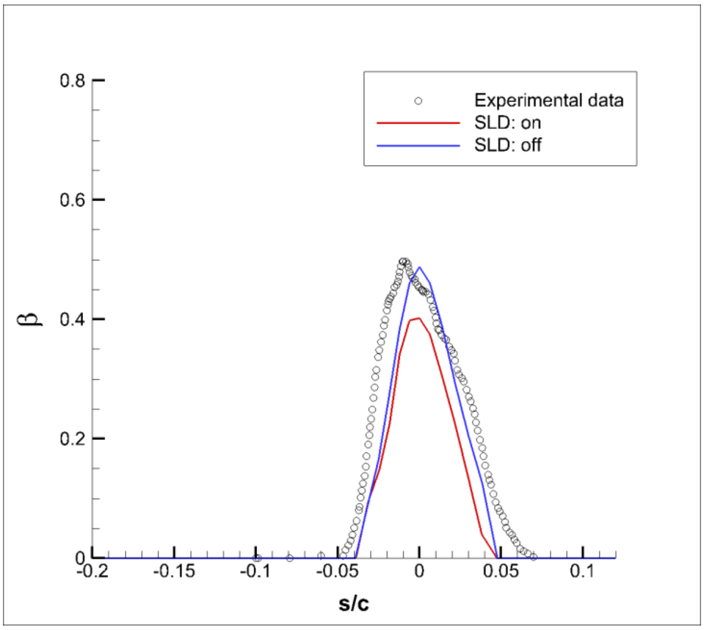

Figure 43: The effects of SLD on collection efficiency (MVD=21 μm, α=0°)

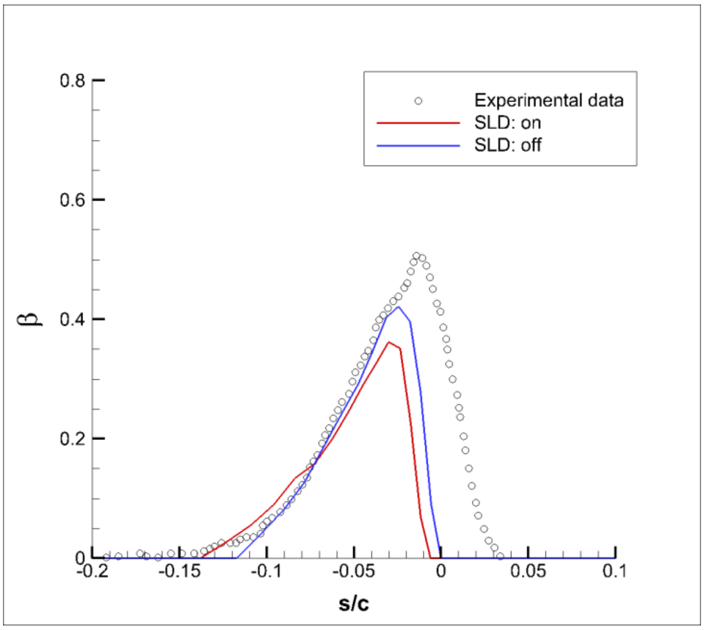

Figure 44: The effects of SLD on collection efficiency (MVD=21 μm, α=8°)

Figure 45 and Figure 46 show collection efficiencies obtained for droplet size of 92 μm at angles of attack of 0° and 8°, respectively. It is clearly seen that including SLD effects into computations reduces collection efficiency due to droplet splash and break-up. On upper surface of the airfoil where s/c>0, agreement is better with experimental data. For both angle of attack cases, "SLD: on" cases yield better collection efficiency predictions, which seems reasonable since MVD is around 100 μm and droplets have SLD characteristics. For non-zero angle of attack case, maximum collection efficiency is observed on the lower surface where s/c<0, as expected.

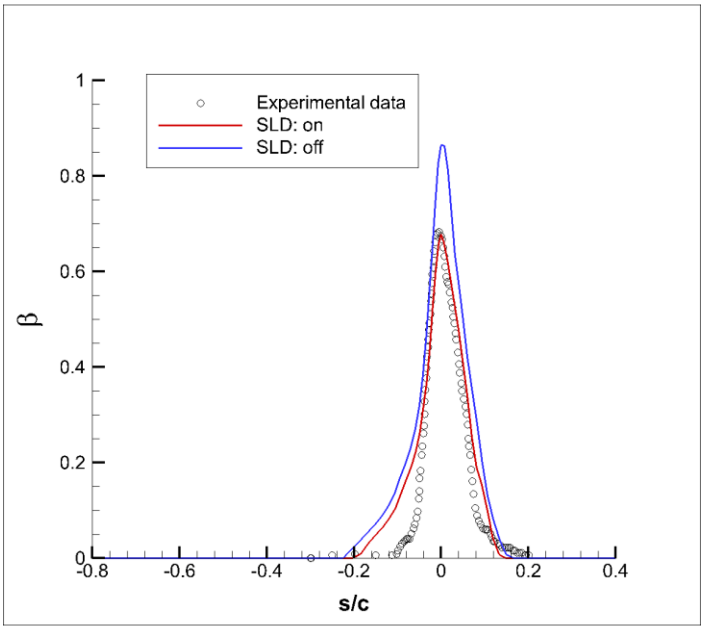

Figure 45: The effects of SLD on collection efficiency (MVD=92 μm, α=0°)

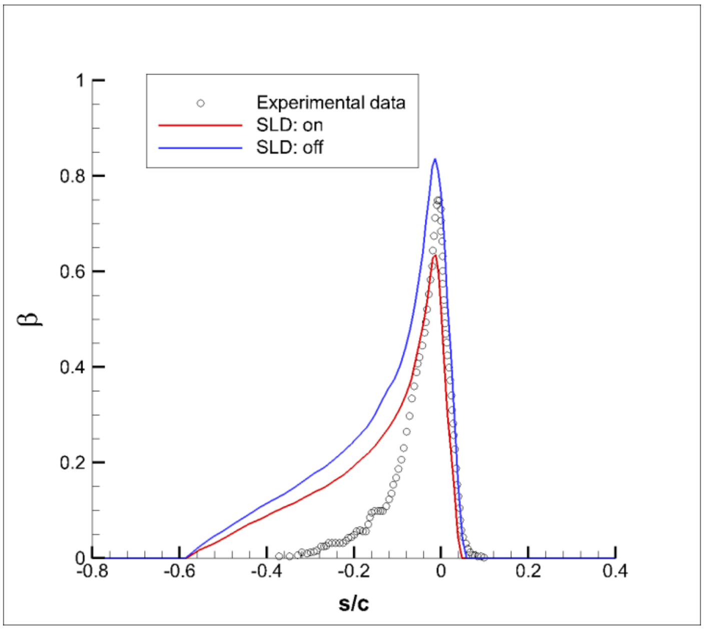

Figure 46: The effects of SLD on collection efficiency (MVD=92 μm, α=8°)

There exists only numerical literature data for collection efficiency with MVD = 236 μm in [32] presented as two models, one of which is Trujillo Model where splashing is taken into account. In the other model, splashing is ignored. The results obtained with these models are compared with "SLD: on" and "SLD: off" results of the current study in Figure 47 and Figure 48.

"SLD: on" results matches with Trujillo model and "SLD: off" results matches with no splashing results quite well especially for the zero angle of attack case. Maximum collection efficiency and its location are predicted successfully.

The results of this section confirm that inclusion of SLD effects significantly improves the results for droplet sizes equal to or greater than 92 μm. The splash model used in the current study is based on experimental data, which is obtained in a geometry and set-up quite different from the geometry and conditions studied here. Therefore, the discrepancy of the results may be partially attributed to this fact.

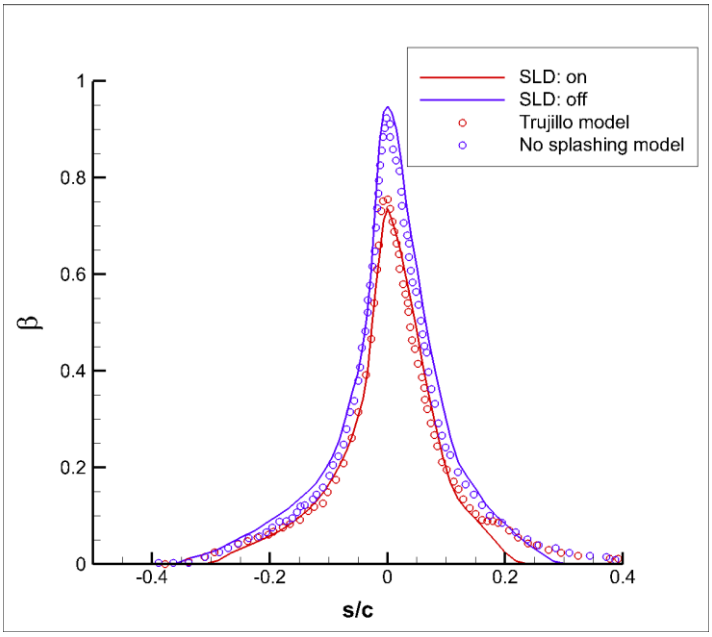

Figure 47: The effects of SLD on collection efficiency (MVD=236 μm, α=0°)

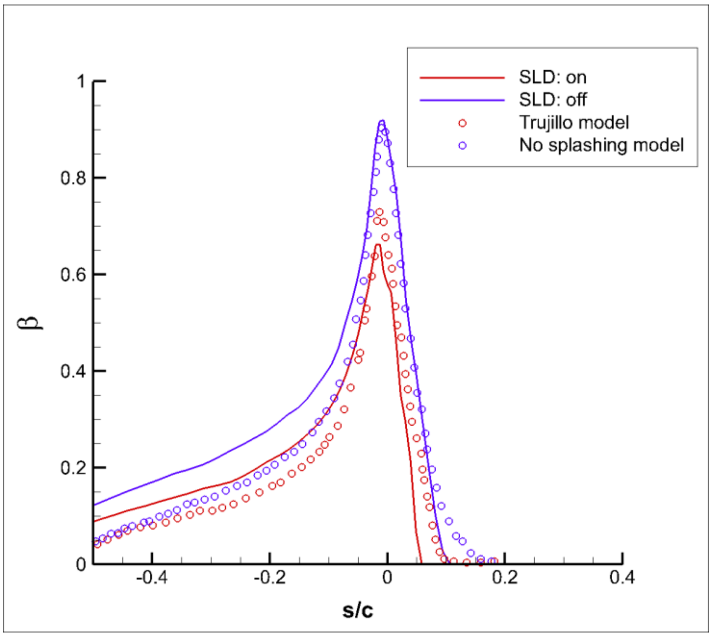

Figure 48: The effects of SLD on collection efficiency (MVD=236 μm, α=8°)

CHAPTER 6

VALIDATION STUDIES ON ENGINE INTAKE GEOMETRIES

In the previous chapter, validation studies are summarized for NACA0012 and MS317 airfoil geometries for various icing conditions, droplet sizes, velocities and exposure times. The effect of SLD characteristics such as droplet splash and break-up are examined. Comparisons with experimental and numerical data available in literature show that the current computational tool is capable of icing simulations on airfoils for a wide range of icing conditions and droplet sizes. Therefore, modifications in the code are applied for intake geometries for 2-D icing simulations. In this chapter, validation studies are presented for axisymmetric and non-axisymmetric engine intake geometries.

6.1. Validation Study for Axisymmetric Engine Intake

2-D icing analyses are performed for an axisymmetric engine intake for zero angle of attack. The intake geometry analyzed is shown in Figure 49 which is presented by Iuliano et al [14]. The external cowl is defined with a super ellipse as:

$$\left(\frac{x}{a}\right)^{n} + \left(\frac{y}{b}\right)^{m} = 1 \tag{73}$$

with

n =1.0; a= 0.2234 m;

m =1.96; b= 0.05448 m.

The inlet lip line is described by an ellipse as:

$$\left(\frac{x}{a}\right)^2 + \left(\frac{y}{b}\right)^2 = 1 \tag{74}$$

with

a= 0.05608 m and b= 0.02243 m.

The length of the inlet is 0.2234 m and its height is 0.1905 m, corresponding to the distance between the inner cowl surfaces at x=0.2234 m, which is the control plane of the inlet.

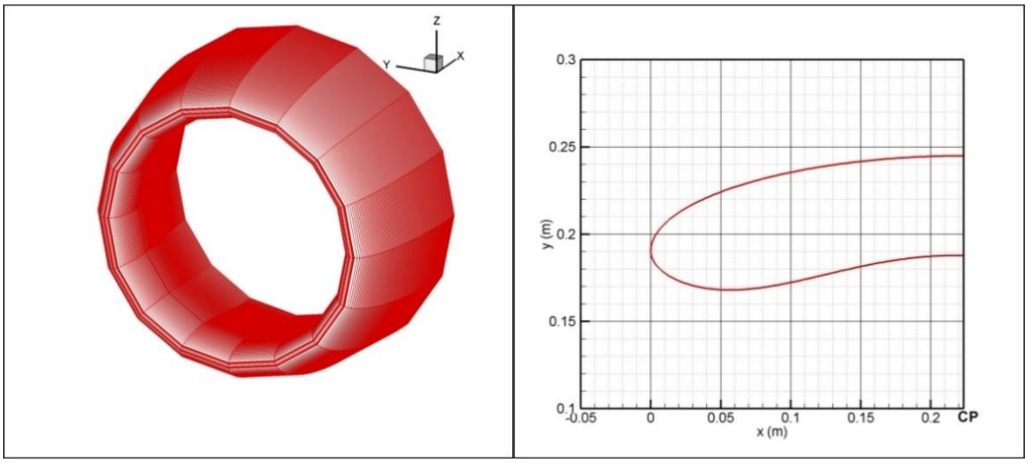

Figure 49: Intake geometry [14]

Table 4: Icing conditions for axisymmetric engine intake

Case #	$\dot{\mathbf{m}}$ $(\mathbf{kg/s})$	MVD $(\mu\mathbf{m})$	LWC $(\mathbf{g/m^3})$	T$_a$ (°C)	Condition
1	10.42	16.45	0.2	-29.9	Rime
2	10.42	20.36	0.2	-29.9	Rime
3	7.8	16.45	0.2	-29.9	Rime
4	7.8	20.36	0.2	-29.9	Rime
5	10.42	16.45	0.695	-9.3	Glaze
6	10.42	20.36	0.695	-9.3	Glaze
7	7.8	16.45	0.695	-9.3	Glaze
8	7.8	20.36	0.695	-9.3	Glaze

Icing conditions for this engine intake are given in Table 4. The velocity is 75 m/s, angle of attack is 0° and exposure time is 30 minutes for all cases. The results are presented in terms of Mach number distributions, collection efficiency distributions, heat transfer coefficients and ice shape predictions. These results are compared with experimental and numerical data provided in [14]. Eulerian approach is utilized in the study of Iuliano et al., whereas Lagrangian approach is used in the current study for the calculation of droplet trajectories.

6.1.1. Flow Field Solution

Figure 50 and Figure 51 depict the Mach number distributions on the intake with $V_\infty = 75\ m/s, \alpha = 0^o$ for $\dot{m} = 10.42\ kg/s$ and $7.8\ kg/s$ obtained by using superposition approach to maintain freestream velocity and desired mass flow rate, which is explained in Chapter 3. As can be seen, the current results are in good agreement with numerical and experimental results given in the literature. Therefore, the flow field solution can be said to be achieved successfully.

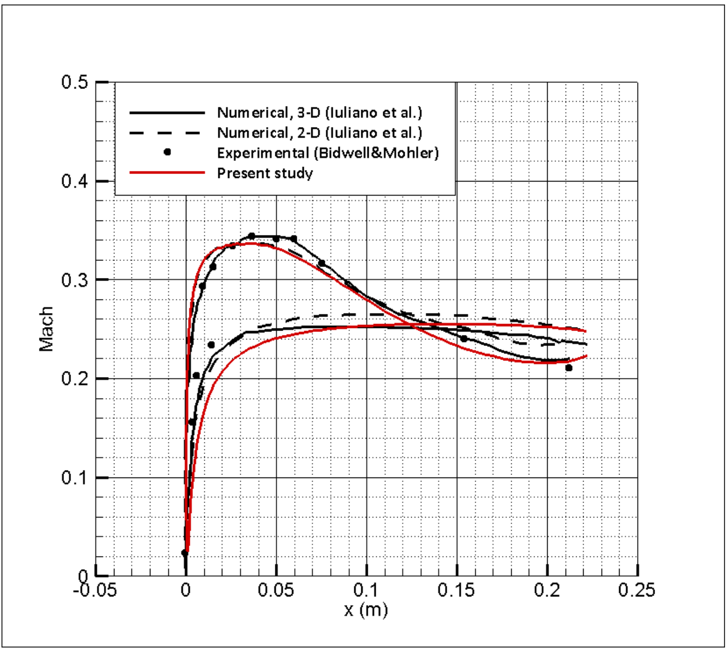

8,

Figure 50: Mach number distribution on the intake for $\dot{m}$ = 10.42 kg/s

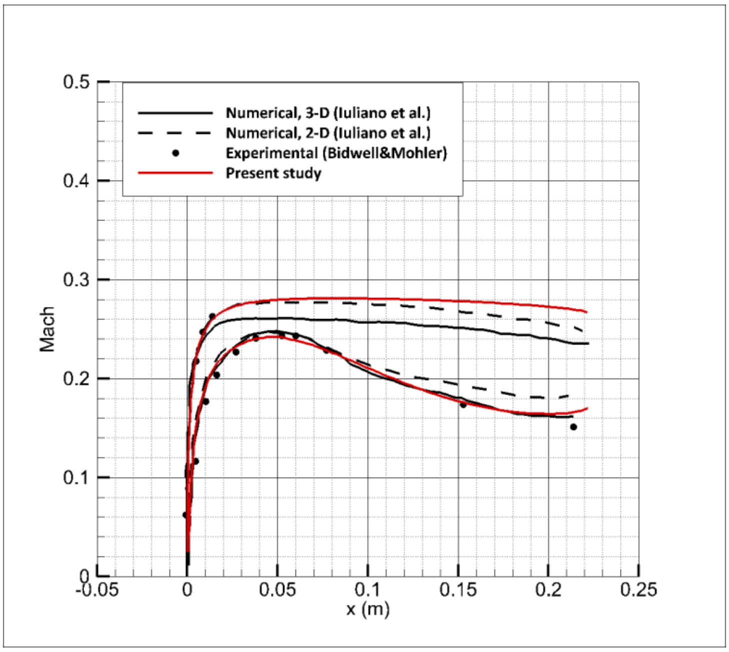

Figure 51: Mach number distribution on the intake $\dot{m}$ = 7.8 kg/s

6.1.2. Droplet Trajectories and Collection Efficiencies

Figure 52 and Figure 53 illustrate collection efficiency results obtained for $\dot{m}$ =10.42 kg⁄s where droplet diameter is 16.45 µm and 20.36 µm respectively. The results are compared with numerical data obtained by Iuliano et al. and experimental data. In the x-axis, negative values represent the inner cowl, while positive values depict the outer cowl. The agreement of the current results with the numerical and experimental data is good. It can also be seen that both the current and Iuliano’s predictions for the maximum value of the collection efficiency are overestimates with respect to the experimental data. Another point worth mentioning is that the impingement zone widens and the maximum collection efficiency increases with increasing droplet size, which is expected. As mentioned in Chapter 2, large droplets have higher inertia and therefore follow more ballistic trajectories, resulting in a wider impingement zone and higher collection efficiency levels.

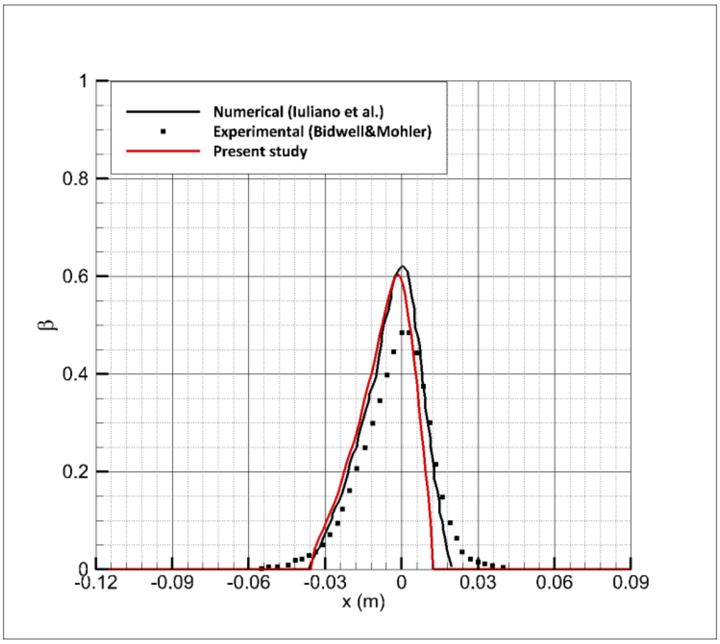

Figure 52: Collection efficiency distribution on the nacelle, α=0°, $\dot{m}$ =10.42 kg⁄s and $d_p = 16.45\ \mu m$

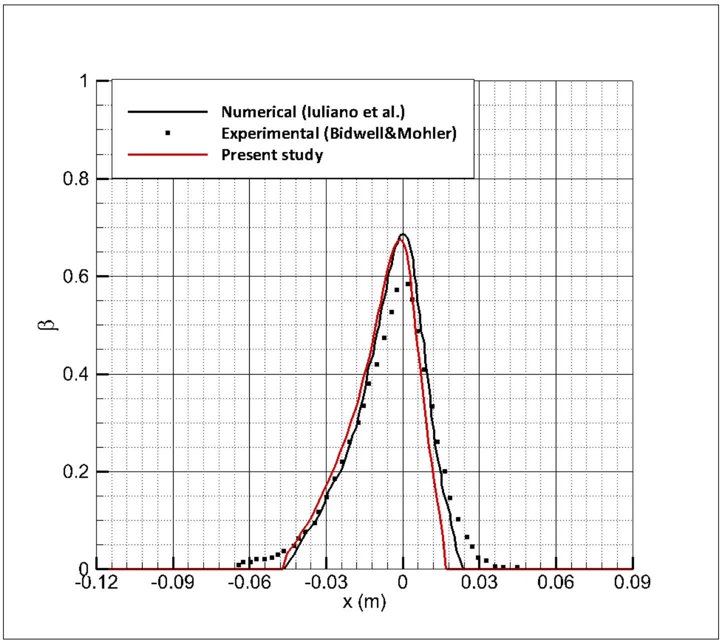

Figure 53: Collection efficiency distribution on the nacelle, α=0°, $\dot{m}$ =10.42 kg⁄s and $d_p = 20.36\ \mu m$

Figure 54 and Figure 55 show the collection efficiency results for ṁ=7.8 kg⁄s where droplet diameter is 16.45 μm and 20.36 μm respectively. As in ṁ=10.42 kg⁄s case, current study results with numerical reference data are quite similar and overestimate the maximum collection efficiency, which are otherwise in good agreement with experimental data.

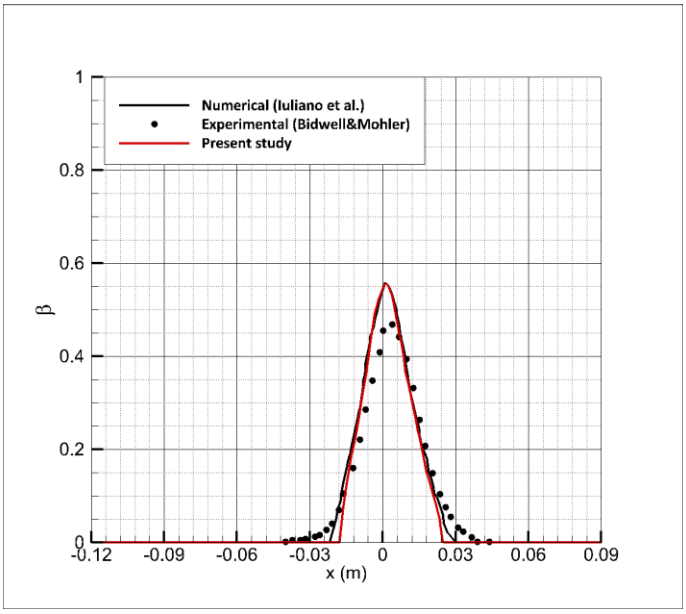

Figure 54: Collection efficiency distribution on the nacelle, α=0°, $\dot{m}$ =7.8 kg⁄s and $d_p = 16.45\ \mu m$

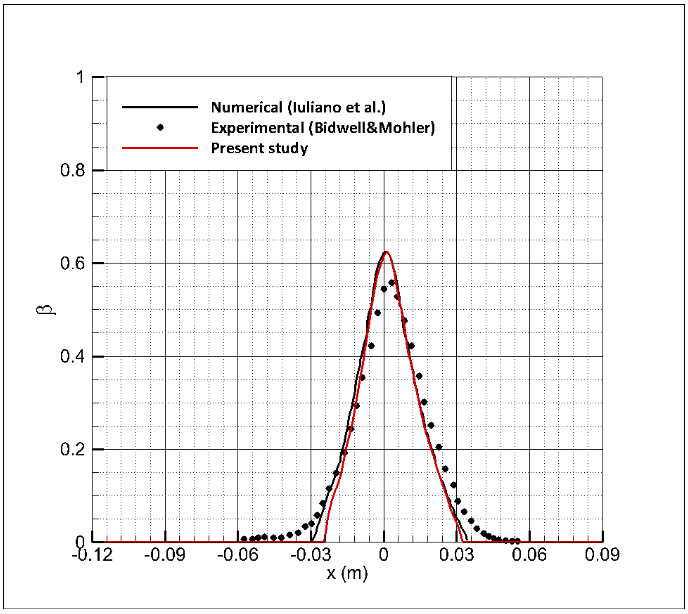

Figure 55: Collection efficiency distribution on the nacelle, α=0°, $\dot{m}$ =7.8 kg⁄s and $d_p = 20.36\ \mu m$

6.1.3. Heat Transfer Coefficients

Figure 56 and Figure 57 show the comparison of the convective heat transfer coefficients obtained with the current approach and numerical data in the literature for two mass flow rates [5]. The agreement of the results is good, which is encouraging for the success of ice accretion simulations because the type and amount of ice that will form on a surface is largely dependent on this parameter.

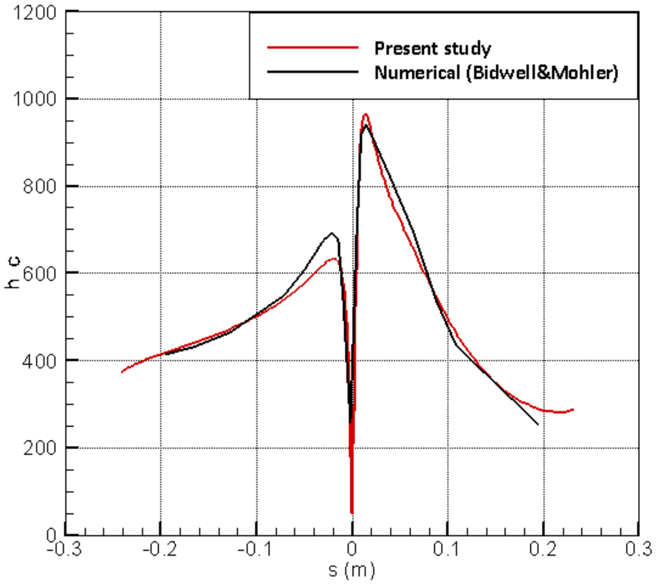

Figure 56: The heat transfer coefficient distribution on the nacelle, $V_\infty = 75\ m/s$,, $\alpha = 0°$ and $\dot{m} = 10.42\ \ kg/s$

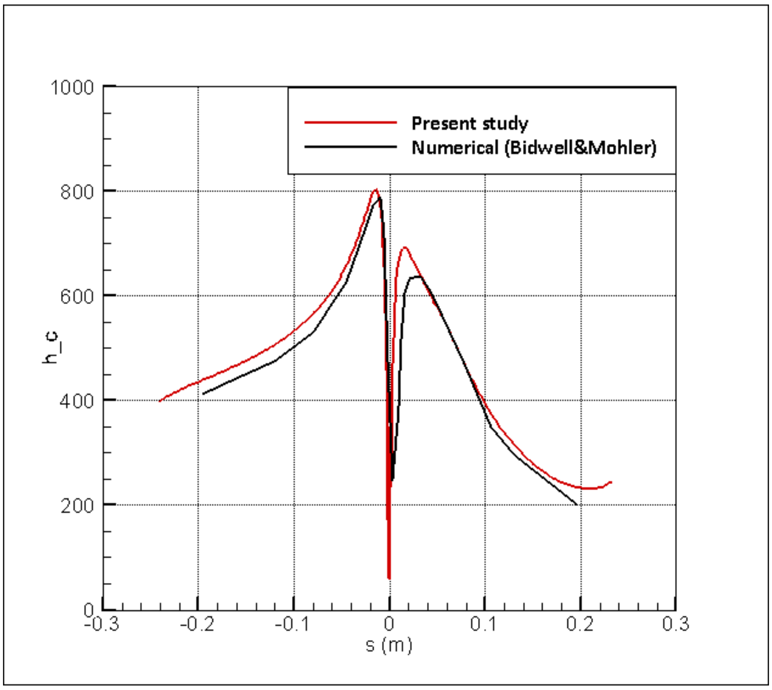

Figure 57: The heat transfer coefficient distribution on the nacelle, $V_\infty = 75\ m/s$, $\alpha = 0°$ and $\dot{m} = 7.8\ \ kg/s$

6.1.4. Ice Shape Predictions

As tabulated in Table 4 there are eight icing cases. The first four cases correspond to rime ice conditions, whereas the remaining cases correspond to glaze ice conditions.

6.1.4.1. Rime ice conditions

Figure 58 to Figure 61 depict the ice shapes corresponding to rime ice conditions. All four shapes are very similar to each other, exhibiting typical rime ice characteristics. Low ambient temperature and liquid water content are responsible for the ice shapes observed. The ice shapes for $\dot{m} = 10.42\ \ kg/s$, are slightly thicker and occupy a wider region compared to the ice shapes for $\dot{m} = 7.8\ \ kg/s$.

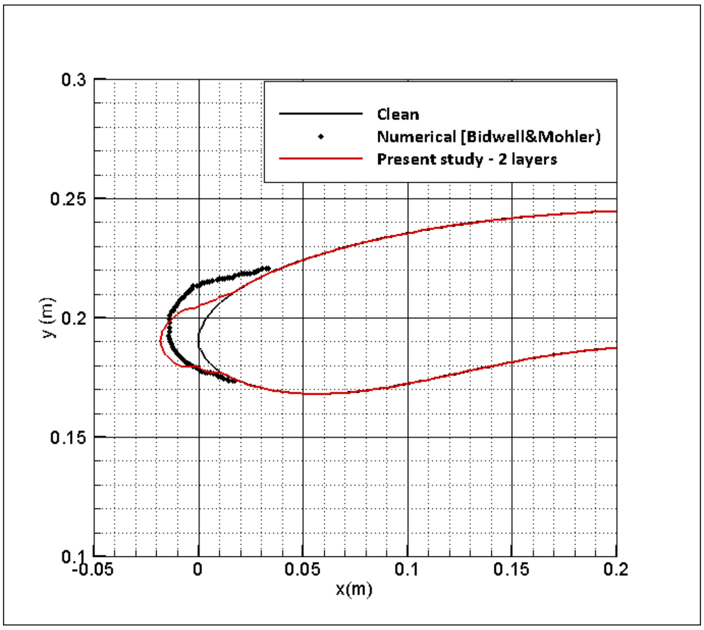

Figure 58: Ice shapes on the air intake, $\dot{m} = 10.42\ kg/s$, $LWC = 0.2\ g/m^3$, $T_a = -29.9°C$ and $d_p = 16.45$ µm

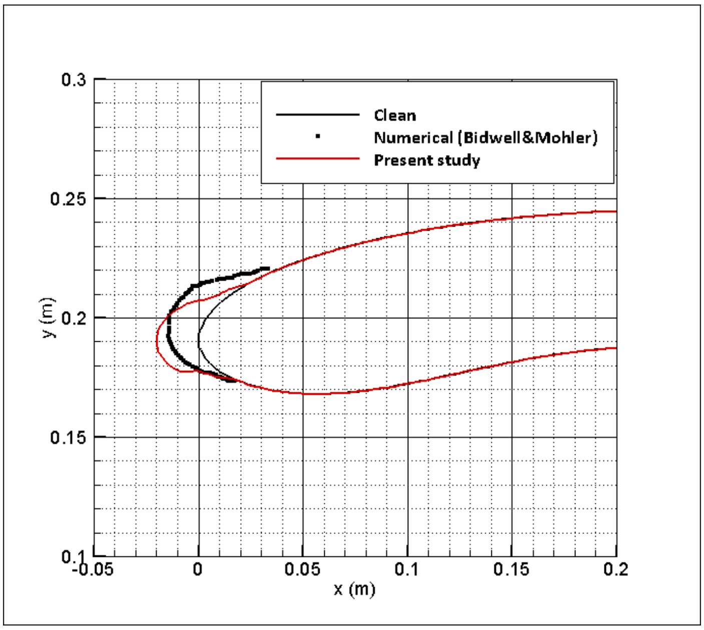

Figure 59: Ice shapes on the air intake, $\dot{m} = 10.42\ kg/s$, $LWC = 0.2\ g/m^3$, $T_a = -29.9°C$ and d_p =20.36 µm

Moreover, the cases with larger droplet sizes lead to a slightly thicker and wider ice shape when one compares $d_p = 16.45$ µm ice shapes with $\mathrm{d_p} = 20.36$ µm shapes. This is in agreement with the collection efficiency results shown in Figure 52 to Figure 55, where large droplets yield slightly higher collection efficiencies and impingement limits. The results of the current study agree fairly well with the literature results both in terms of the overall ice shapes and ice masses. The current study underestimates the extent of ice on the upper surface, while the maximum ice thickness is significantly overpredicted. However, the ice masses that are predicted by the current study and the literature are roughly similar. It also has to be pointed out that the numerical data used for comparison dates back to 1995, and are obtained from a small, low resolution graph, which may partly explain the discrepancy. The results are obtained using 2 computational steps for rime ice calculations.

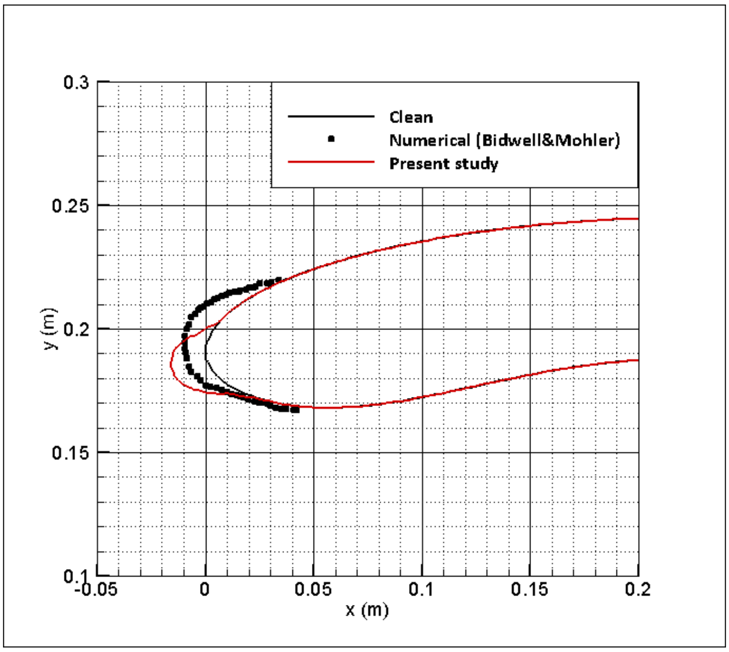

Figure 60: Ice shapes on the air intake, $\dot{m} = 7.8\ kg/s$, $LWC = 0.2\ g/m^3$, $T_a = -29.9°C$ and d_p =16.45 µm

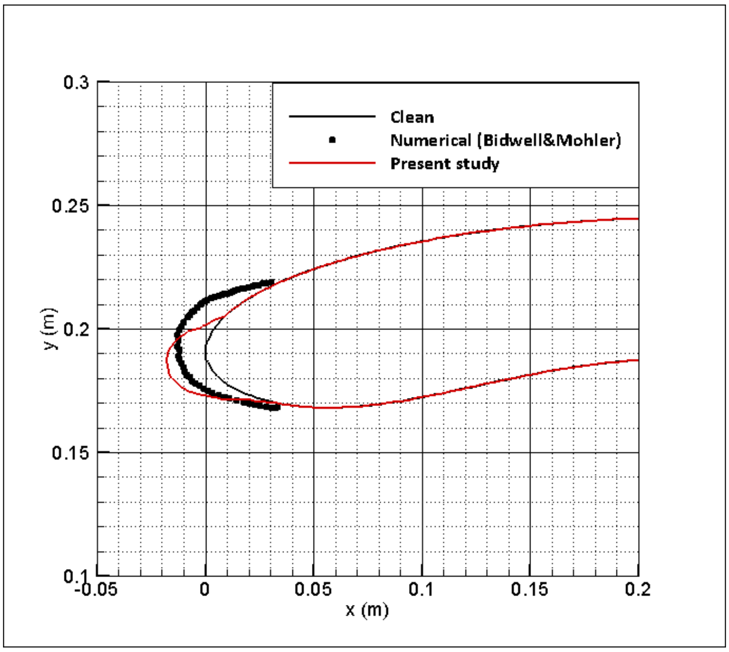

Figure 61: Ice shapes on the air intake, $\dot{m} = 7.8\ kg/s$, $LWC = 0.2\ g/m^3$, $T_a = -29.9°C$ and $d_p = 20.36$ µm

6.1.4.2. Glaze ice conditions

Figure 62 to Figure 65 depict the ice shapes corresponding to glaze ice conditions. All four shapes exhibit two horn shapes, which are typical glaze ice features. High ambient temperature and high liquid water content are responsible for the ice shapes observed. These horns ae also present in the numerical literature data. However, the agreement is only qualitative, since the magnitudes and locations of the horns are only superficially similar in the two predictions. Due to the lack of experimental data, it is not possible to comment on the accuracy of either solution. Comparing these ice shapes with the ones obtained in rime ice conditions, it is seen that the glaze ice shapes are highly irregular and such a shape would be more detrimental to aerodynamic performance and intake performance.

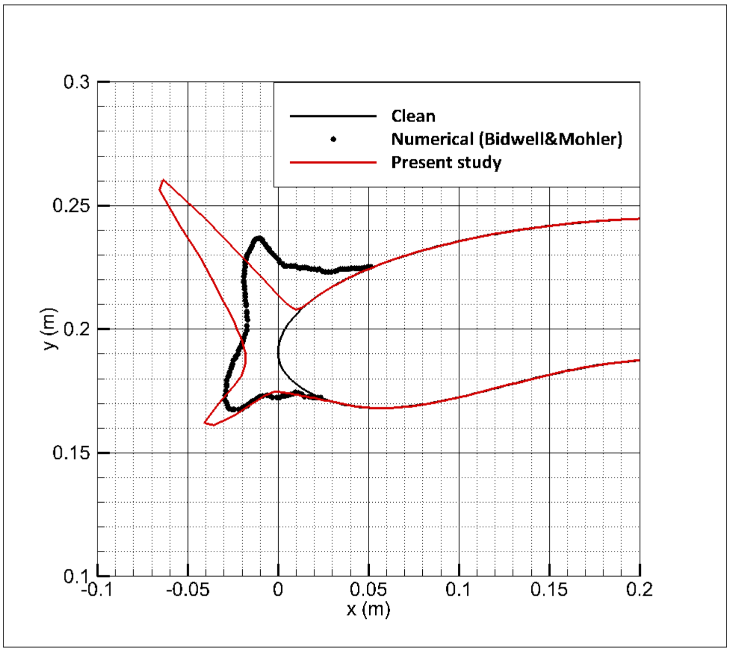

Figure 62: Ice shapes on the air intake, $\dot{m} = 10.42\ kg/s$, $LWC = 0.695\ g/m^3$, $T_a = -9.3°C$ and $d_p = 16.45$ μm

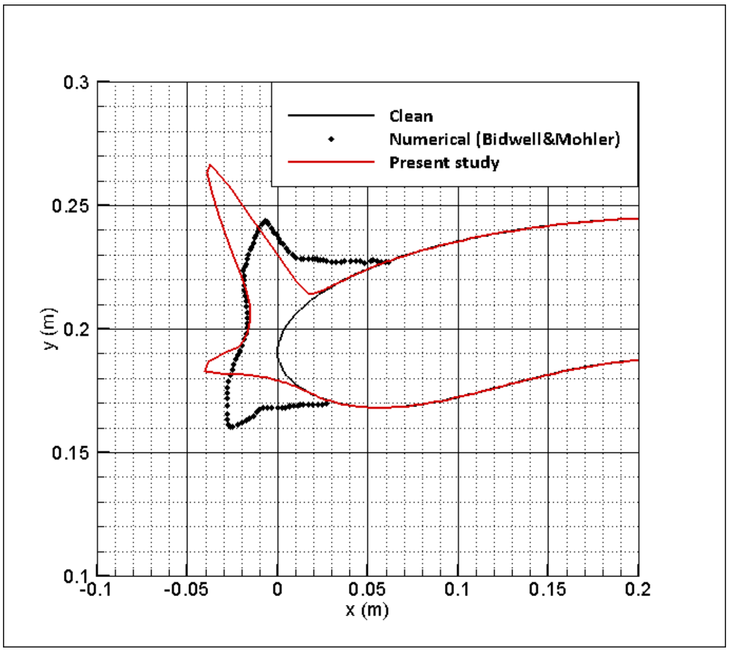

Figure 63: Ice shapes on the air intake, $\dot{m} = 10.42\ kg/s$, $LWC = 0.695\ g/m^3$, $T_a = -9.3°C$ and $d_p = 20.36$ μm

When the ice shapes for the same mass flow rate but different droplet sizes are compared, it is observed that the ice shape for larger droplets is also slightly larger and thicker. This is also in agreement with the collection efficiency distributions in Figure 53 to Figure 57. Also, the ice shapes for $d_p = 16.45$ μm are equally spread in the upper and lower surfaces but the ice shape for $d_p = 20.36$ μm is mostly on the upper surface. Although the droplet sizes are similar, their trajectories and consequently collection efficiencies are sufficiently different to yield dissimilar ice shapes.

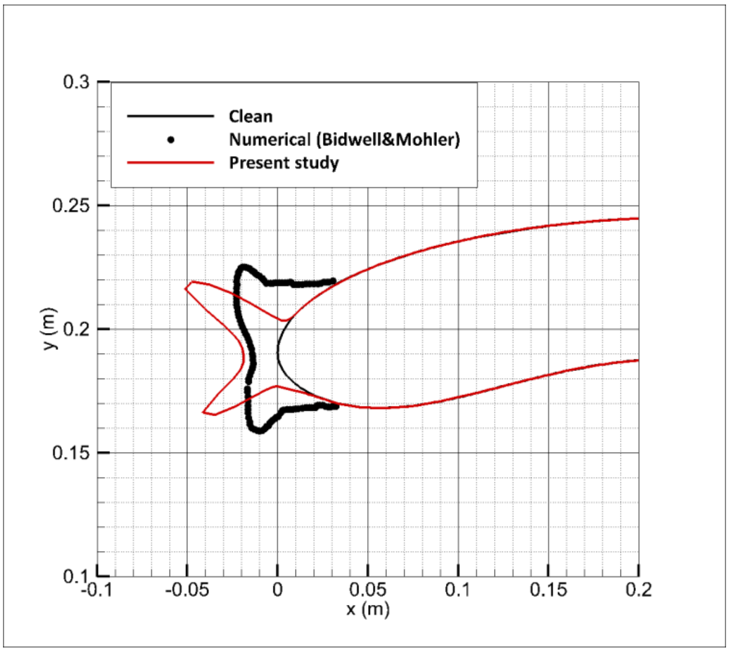

Figure 64: I Ice shapes on the air intake, $\dot{m} = 7.8\ kg/s$, $LWC = 0.695\ g/m^3$, $T_a = -9.3°C$ and $d_p = 16.45$ μm

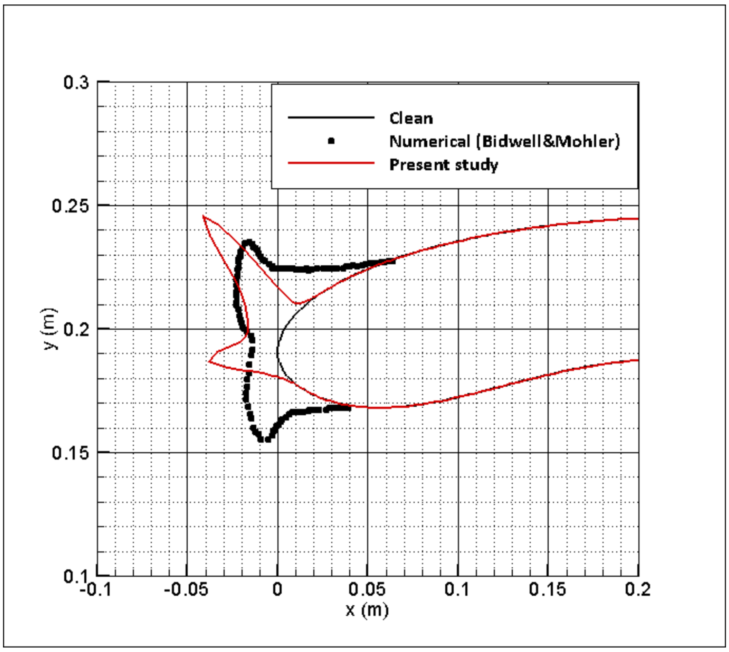

Figure 65: Ice shapes on the air intake, $\dot{m} = 7.8\ kg/s$, $LWC = 0.695\ g/m^3$,

$T_a = -9.3°C$ and $d_p = 20.36$ μm

Icing analyses for glaze ice conditions are obtained with 10 layers of computation. As mentioned before, for glaze ice cases higher number of steps is required due to the need for representing runback water phenomena more faithfully.

In this validation study, results for flow field, droplet trajectories, convective heat transfer coefficients and ice shape predictions are presented and compared. The agreement in results with reference numerical and experimental data helped to verify that the proposed approach for maintaining the mass flow rate through the inlet is valid.

In order to improve glaze ice predictions, a better runback water model can be applied to the existing code. In the current approach, all unfrozen water in a panel is assumed to run back to the next downstream panel which might be an over-simplified assumption.

6.1 Validation Study for Non-Axisymmetric Engine Intake

6.1.1 Intake Geometry

The intake geometry shown in Figure 66 is studied, which is presented in the study of Shen et al [28]. Due to the lack of coordinates of the commercial intake geometry, they are obtained by digitizing 2-D view given in [28] shown in Figure 66. In order to obtain smooth outlines, outer and inner cowls are defined by a super ellipse and ellipse. The intake is non-axisymmetric with an inlet length of 0.824 m and duct height of 1.44 m which as shown in Figure 67.

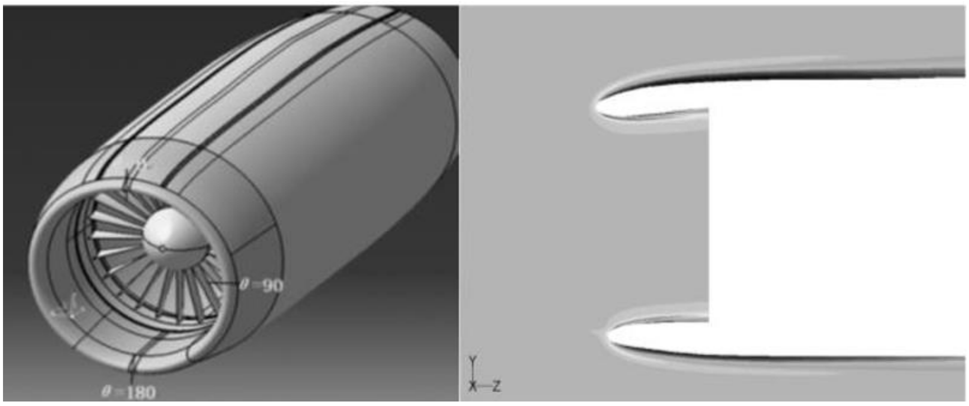

Figure 66: 3-D view (on the left) and 2-D view (on the right) of the commercial engine intake geometry studied [28]

As explained in Flow Field Solution section in Chapter 3, superposition approach [38] is utilized to maintain both desired flight condition and mass flow rate at the control plane. In this method, the panel geometry is modified as shown in Figure 67 by extending the trailing edge panels in x-direction in order to avoid unrealistic velocity gradients at the trailing edge.

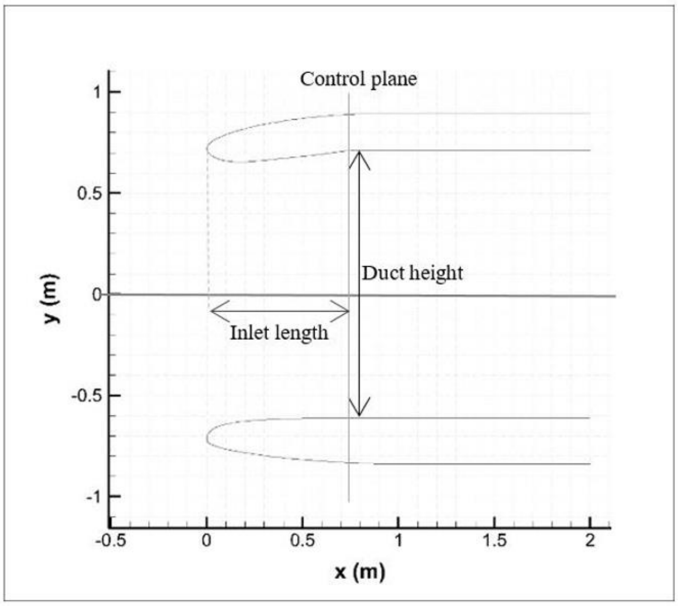

Figure 67: Modified intake geometry for panel method with constant diameter

6.1.2 Results and Discussion

Predicted ice shape and collection efficiency results are presented for the commercial aircraft intake geometry. The results are compared with the numerical data presented by Shen et al [28], which are obtained with FENSAP-ICE commercial tool and a code developed by the authors. Icing conditions for which the analyses are performed are listed in Table 5. There are two icing conditions for different temperature values of 253 K and 263 K.

Table 5: Icing conditions for validation study of non-axisymmetric engine intake

Mach	**Pressure (Pa)**	**Angle of attack (°)**	**MVD (µm)**	**LWC (g/m³)**	**ṁ (kg/s)**	**Temperature (K)**	**Exposure time (s)**
0.4	101325	3	20	1	200	253 and 263	420

Ice shape results for T=253 K are given in Figure 68 and Figure 69 for upper and lower lips of the intake, which are stated as θ=0° and θ=180° respectively in Figure 66.

For the upper surface, accumulated ice is predicted smaller when compared to reference numerical data. Impingement limits differ for current study and reference data. Current study results show a smaller region occupied by the accumulated ice. However, ice shape can be said to be similar to the one obtained by Shen et al although the limits are underestimated.

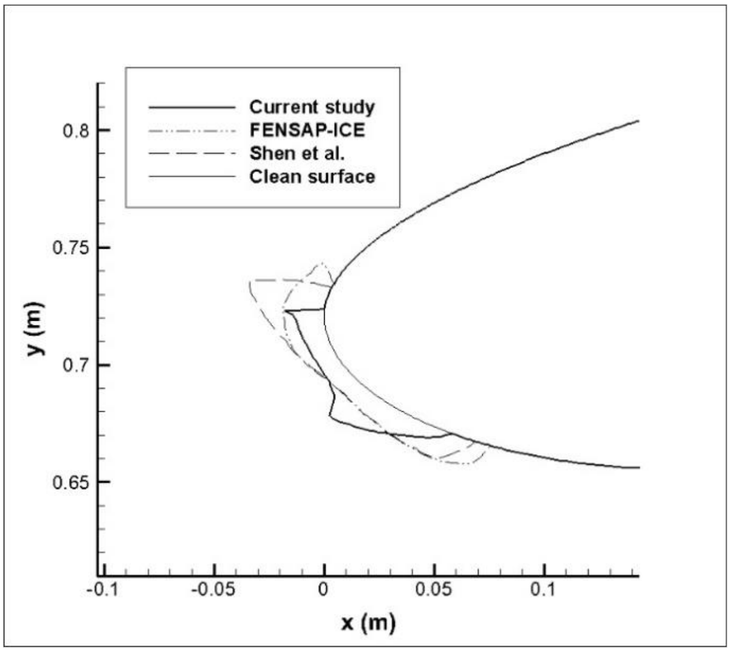

Figure 68: Ice shape prediction on the upper lip at $T = 253\ K$

In Figure 69, ice shape is given for the lower lip of the intake. It is observed that impingement limit in the lower part of the lip is predicted the same with the reference numerical data although the upper impingement limit is estimated different which leads to the prediction of the iced region to be smaller for the current study. Ice thickness is predicted very similar when compared to reference numerical data except for the sharp section in the upper region of the leading edge. It is clear that flow field is affected by the ice accumulated on the lower surface since the angle of attack is 3^o.

Therefore, ice shape predicted on the lower surface will have an effect on ice shape on the upper surface as well. It can be deduced that the sharp ice section accumulated on the lower surface may lead the ice mass on the upper surface to be underestimated.

The second flight condition at which the icing analysis are performed is at $T = 263\ K$. Since the ambient temperature is high, unfrozen liquid acts like runback water and freezes downstream on the surface.

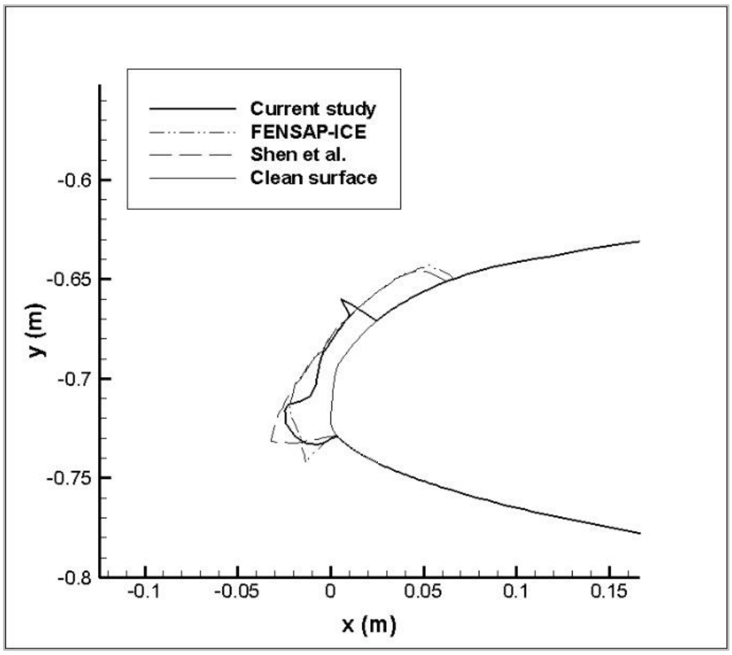

Figure 69: Ice shape prediction on the lower lip at $T = 253\ K$

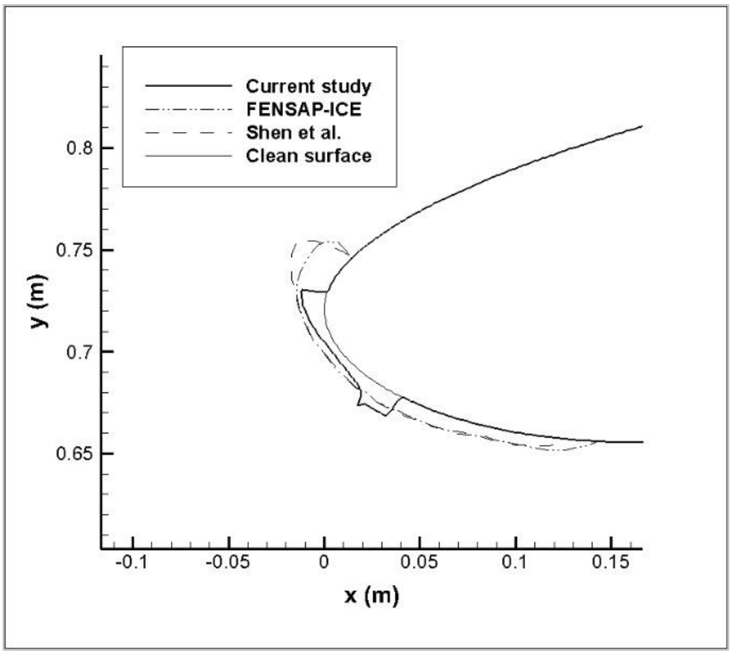

Figure 70: Ice shape prediction on the upper lip at $T = 263\ K$

Figure 70 depicts ice shape predictions on the upper surface for $T = 263\ K$. Ice shape can be said to be similar considering the sharp edge on the top and the ice thickness for the current study result and reference numerical data. However, it is observed that impingement limits especially in lower part are estimated poorly in the present study.

In Figure 71, ice shape results on the lower surface are presented. Similar to upper surface, impingement limits are not predicted well compared to reference results. Ice thickness is estimated thicker in the current study. The ice shape is horn-like shape in which is a glaze ice characteristic; however, it is quite different than reference numerical data.

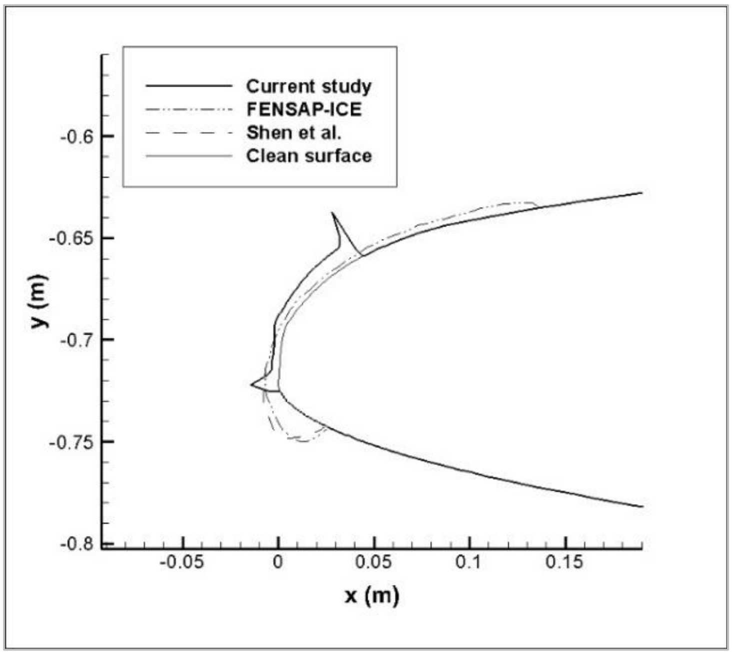

Figure 71: Ice shape prediction on the lower lip at $T = 263\ K$

Multi-step calculation approach is used in the icing analyses. In this approach, the exposure time is divided into shorter intervals and the computational procedure is repeated for each interval. At the beginning of each interval, iced surface is considered as the new geometry. In previous studies of the authors [24], [25], it is observed that multi-step calculation approach improves ice shape predictions as exposure time increases and for especially glaze ice conditions. On the other hand, after trying different numbers of calculation steps for the engine intake icing analyses, it is noticed that single-step calculation gives the best ice shape result. The inconsistency between the results of the previous studies and the current study in terms of multi-step approach is a sign of a possible error in the computations which may lead to poor ice shape predictions. The modules of the developed code are needed to be checked and improved if necessary in order to enhance the ice shape results.

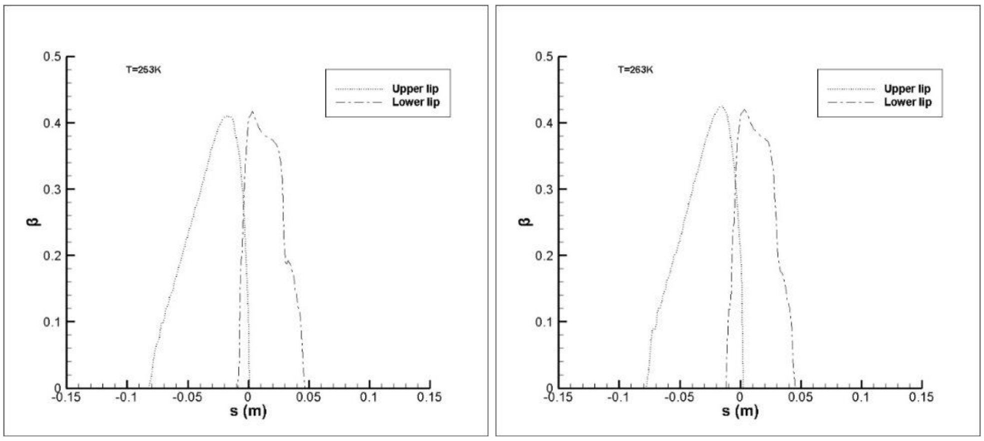

Figure 72: Collection efficiency (β) on upper and lower lips at $T = 253\ K$ (on the left) and $T = 263\ K$ (on the right)

As mentioned in Methodology section, Lagrangian approach is utilized for droplet trajectory calculations. Collection efficiency distribution on upper and lower lips are presented in Figure 72 for $T = 253\ K$ and $T = 263\ K$. Negative s values represent lower part of the lip whereas positive s values represent upper part of the lip. Collection efficiencies for two cases are very similar. Maximum collection efficiency, β, is calculated as around 0.42 which is observed at the stagnation point of the intake lip for both cases. In the reference paper by Shen et al. [28], maximum collection efficiency is said to be found as 0.42 with Eulerian approach without indicating the flight condition. Despite different trajectory methods, maximum collection efficiency values are found the same. Lack of collection efficiency distribution in the reference data prevents further comparisons to be done.

CHAPTER 7

CONCLUSION AND FUTURE WORK

The purpose of this study is to develop a computational tool which will be utilized for icing analysis on engine nacelles both for certification purposes and anti/de-icing system design.

Modules for flow field solution, droplet trajectory and collection efficiencies, thermodynamic analysis and ice accretion comprise the developed tool. Validation studies are performed for 2-D wing geometries, axisymmetric and non-axisymmetric engine intake geometries. Ice shape prediction and collection efficiency results obtained for airfoils and axisymmetric engine intake show good agreement with reference numerical and experimental data. Therefore, it is deduced that the approach employed in the computational tool is applicable for axisymmetric engine intake geometries. On the other hand, relatively poor agreement is obtained between reference numerical data and current study results for ice shapes in validation study on non-axisymmetric engine geometry. The inconsistency could be stemmed from a possible error in the computations. Therefore, the modules which constitute the developed computational tool must be checked in order to improve the results.

To sum up, the developed tool is capable of predicting ice accumulation for given icing conditions on engine intakes for axisymmetric cases. As seen from airfoil validation studies, SLD effects are successfully included which means that icing analysis can be performed for a wide range of droplet sizes extending beyond Appendix C conditions.

Extension of the current computational tool to handle solid and mixed-phase icing cloud conditions will be a reasonable future work since they have become an interest for certification purposes lately. Such meteorological conditions are closely relevant to engine geometries because solid cloud particles become an icing threat on heated components, like engines. Some modifications are needed to be considered to include solid and mixed-phase icing cloud conditions. Drag law must be modified in such a way that the effect of non-spherical particle shape on drag force is taken into account. For ice crystal trajectories in heated environments, heat transfer between the crystal and the surroundings has to be considered, as well as phase change of particles. In addition to these, impingement models and ice accretion models need to be updated.

The splash model used in the current study is based on experimental data which is obtained in a geometry and set-up quite different from the geometry and conditions studied here. The discrepancy of the results may be partially attributed to this fact. In order to enhance the results, an SLD model based on a new database is required for a to model SLD behavior better.

REFERENCES

[1] Advisory Group For Aerospace Research & Development (AGARD), Ice Accretion Simulation, AGARD-AR-344, 1998.

[2] Al-Khalil, Keith Jr, T.G., De Witt, K.J. Icing calculations on a typical commercial jet engine inlet nacelle, *J. Aircraft* 34 (1), p. 87-93, 1997.

[3] Beaugendre, H., Morency, F., Habashi, W.G., FENSAP-ICE' s Three-Dimensional in-flight ice accretion module: ICE3D, *J. Aircraft* (40)2, 239-247, 2003.

[4] Bidwell, C.S., Particle trajectory and icing analysis of the E3 turbofan engine using LEWICE3D Version 3, NASA TM-217696, 2012.

[5] Bidwell, C.S. and Mohler, S.R. Jr., Collection efficiency and ice accretion calculations for a sphere, a swept MS(1)-317 wing, a swept NACA 0012 wing tip, an axisymmetric inlet and a Boeing 737-300 inlet, AIAA 95-0755, 1995.

[6] Bourgault, Y., Boutanios, Z., Habashi, W.G., Three-dimensional Eulerian approach to droplet impingement simulation using FENSAP-ICE, Part 1: model, algorithm and validation, *J. Aircraft* 37(1), p. 95-103, 2000.

[7] Clift, R., Grace, J.R., and Weber, M.E., *Bubbles, Drops and Particles*, Academic Press, New York, 1978.

[8] Cossali, G.E., Coghe, A., and Marengo, M., *The impact of a single drop on a wetted solid surface, Exp. Fluids,* Vol. 22, 1997.

[9] Dima, C., Brandi, V., Prediction of ice accretion on airfoils using CIRA multi-ice code, NATA/RTO Workshop Report, December 2000.

[10] Gent, R.W., Dart, N.P. and Cansdale, J.T., Aircraft Icing, Phil. Trans. R. Soc. Lond. A, Vol. 358, p: 2873-2911, 2000.

[11] Hamed, A., Das, K., Basu D., Numerical simulations of ice droplet trajectories and collection efficiency on aeroengine rotating machinery, AIAA-2005-1248, in *AIAA Aerospace Sciences Meeting and Exhibit, Reno, USA*, 2005.

[12] Hirt, C. W., Nicholls, B. D., "Volume of Fluid Method for Dynamic Free Boundary," *J. Comp. Phys.*, v.39, 1981.

[13] Intakes. http://training.deicinginnovations.com/?page_id=622/. Accessed: 2017-07-10.

[14] Iuliano, E., Mingione, G., de Domenico, F., de Nicola, C., An Eulerian approach to three-dimensional droplet impingement simulation in icing environment, *AIAA Guidance, Navigation and Control Conference, Toronto,* AIAA 2010-7077, 2010.

[15] Myers, T.G., Extension to the Messinger Model for aircraft icing, *AIAA J.* 39(2), 211-218, 2001.

[16] Ogretim,E., Huebsch, W., Shinn, A., Aircraft Ice Accretion Prediction Based on Neural Networks, *Journal of Aircraft*, Vol. 43, No. 1, January–February, 2006.

[17] Özgen, S., Canıbek, M., Korkem, B. and Ortakaya, Y., Ice shape prediction on airfoils using Extended Messinger method, in *4th Ankara International Aerospace Conference, Ankara, Turkey,* 2007.

[18] Özgen, S., Canıbek, M., Ice accretion simulation on multi-element airfoils using Extended Messinger Model, *Heat and Mass Transfer* 45, p. 305-322, 2009.

[19] Özgen, S., Canıbek, M., In-flight icing prediction with high speed flow effects, in *HEFAT 2012-9th International Conference on Heat transfer, Fluid Mechanics and Thermodynamics, Malta,* 2012.

[20] Özgen, S., Tarhan, E., Canıbek, M., Parallel computing applied to three-dimensional droplet trajectory simulation in Lagrangian approach, 2011-38-0106, in *SAE 2011 International Conference on Aircraft and Engine Icing and Ground Deicing, Chicago, USA*, 2011.

[21] Özgen, S., Tarhan, E., Canıbek, M., 3-D in-flight icing simulations and use of parallel computing in Lagrangian droplet trajectory calculations, in *6th Ankara International Aerospace Conference, Ankara, Turkey*, 2011.

[22] Özgen, S. Canıbek, M., In-flight ice formation simulation on finite wings and air intakes, *Aeronautical J.* 116(1177), p. 337-362, 2012.

[23] Özgen, S., Canıbek, M., Tarhan, E., Lagrangian droplet impingement analysis and validation for a swept wing, in *5th European Conference for Aeronautics and Space Sciences (EUCASS), Munich, Germany,* 2013.

[24] Özgen, S., Uğur, N., Görgülü, İ. and Tatar, V., Ice Accretion Prediction on an Engine Inlet, in *Ankara International Aerospace Conference (AIAC), Ankara*, 2015.

[25] Özgen, S., Uğur, N., Görgülü, İ. and Tatar, V., Ice Accretion Prediction on Engine Nacelles in Liquid Phase Clouds, in *SAE International Conference on Icing of Aircraft Engines and Structures, Prague,* 2015.

[26] Papadakis, M., Hung, K.E., Vu, G.T., Wei Yeong, H., Bidwell, C., Breer, M., Bencic, T.J., Experimental investigation of water droplet impingement on airfoils, finite wings and S-duct engine inlet, NASA TM-211700, 2002.

[27] Paraschiviou, I., Saeed, F., Aircraft Icing, John Wiley & Sons, New York, 2007

[28] Shen, X., Lin, G., Yu J., Bu X., and Du C., Three-Dimensional Numerical Simulation of Ice Accretion at the Engine Inlet, *Journal of Aircraft,* Vol. 50, No. 2, 2013.

[29] Trapaga, G. and Szekely, J., Mathematical modeling of the isothermal impingement of liquid drops in the spraying process, *Metallurgical Transactions B,* v. 22B, pp. 901-914, 1991.

[30] Veillard, X., Habashi, W.G., Aube, M.S, Baruzzi, G.S, FENSAP-ICE, Ice accretion in multi-stage jet engines, in *19th AIAA Computational Fluid Dynamics Conference, San Antonio, USA,* 2009.

[31] Wright, W.B., and Potapczuk, M.G., Computational Simulation of Large Droplet Icing, Proceedings of the FAA International Conference on Aircraft Inflight Icing, 1996.

[32] Wright, W.B., Potapczuk, M.G., Semi-empirical modeling of SLD physics, NASA TM-2004-212916, 2004.

[33] Wright, W.B., Validation results for LEWICE 3.0, NASA CR-2005-213561, 2005.

[34] Wright,W.B. Further refinement of the LEWICE SLD model, NASA CR-2006-214132, 2006.

[35] Wright W.B., Gent R.W., Guffond D., DRA/NASA/ONERA Collaboration on Icing Research Part II- Prediction of Airfoil Ice Accretion, NASA CR-202349, 1997.

[36] Wright W.B., User’s Manual for LEWICE Version 3.2, NASA CR-2008-214255, 2008.

[37] Wright,W.B, Jorgenson, P.C.E., Veres, J.P., Mixed phase modeling in GlennICE with application to engine icing, AIAA 2010-7674, in *AIAA Guidance, Navigation, and Control Conference, Toronto, Canada,* 2010.

[38] Waung, T.S., *An ejector inlet design method for a novel rocket-based combined cycle rocket nozzle,* M.Sc. Thesis, Ottawa-Carlton Institute for Mechanical and Aerospace Engineering, 2010.